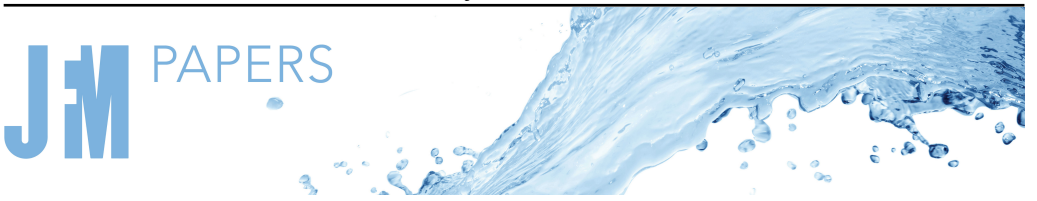
J. Fluid Mech. (2026), *vol.* 1045, A11, doi:10.1017/jfm.2026.12068



Low-frequency oscillations of shock wave/turbulent boundary layer interaction over a vibrating panel

Hengyu Cai[1,2], **Ming Yu**[3], **Bo Li**[3], **Dong Sun**[3], **Zhengyin Ye**[1,2] and **Xianxu Yuan**[3]

[1]School of Aeronautics, Northwestern Polytechnical University, Xi'an, Shaanxi 710072, PR China

[2]National Key Laboratory of Aircraft Configuration Design, Xi'an 710072, PR China

[3]State Key Laboratory of Aerodynamics, Mianyang 621000, PR China

Corresponding authors: Dong Sun, sund1986@foxmail.com; Zhengyin Ye, yezy@nwpu.edu.cn

(Received 7 January 2026 UTC; revised 17 August 2026 UTC; accepted 22 August 2026 UTC)

This study employs direct numerical simulations to investigate the influence of a vibrating wall panel on the oblique shock wave/turbulent boundary layer interaction flows at incoming free-stream Mach number 2.9. We examine two distinct low-frequency vibration modes, defined by their streamwise deformation patterns: a full-panel (symmetric) mode and a half-panel (antisymmetric) mode. By analysing phase-average flow quantities, we demonstrate that the antisymmetric mode primarily forces a streamwise oscillation of the separation bubble, whereas the symmetric mode amplifies its inherent expansion–contraction ('breathing') motion. Both panel vibrating modes enhance quasi-periodic shock oscillation and modulate the plateau in the mean wall pressure distributions. Spectral analysis confirms that low-frequency pressure fluctuations are amplified not only at the mean separation point but also in the mid-region of the panel. Through correlation analysis and dynamic mode decomposition, we establish that these vibrations lead to strong spatiotemporal coherence, associating upstream fluctuations near the separation to downstream propagation. Critically, a comparative analysis reveals that the symmetric mode facilitates significantly longer downstream propagation of pressure disturbances than the antisymmetric mode. This highlights how the spatial pattern of panel deformation, not just the vibration frequency, modulates the unsteady flow characteristics.

Key words: shock waves, turbulent boundary layers, flow-structure interactions

© The Author(s), 2026. Published by Cambridge University Press.

https://doi.org/10.1017/jfm.2026.12068 Published online by Cambridge University Press

1. Introduction

Shock wave/turbulent boundary layer interaction (STBLI) occurs widely in the internal and external flows of high-speed aircraft. It can generate local strong pressure fluctuations, which may lead to structural vibration, fatigue or even structural failure (Dolling 2001; Gaitonde 2015), seriously impacting the aerodynamic performance and structural safety of the aircraft. Therefore, investigating the physical characteristics of pressure fluctuations in STBLI is crucial for the design and optimisation of high-speed aircraft.

In STBLI, the adverse pressure gradient induced by strong shock waves causes significant flow deceleration in the boundary layer and flow separation (Delery 1985; Wang *et al.* 2016, 2019), thereby complicating the unsteady characteristics of the pressure fluctuations. This unsteady behaviour has remained at the forefront of STBLI research for decades (Dupont *et al.* 2006; Wu & Martin 2007; Ringuette *et al.* 2009), with numerous investigations dedicated to unravelling its origins yet yielding no universally accepted explanation. These can be summarised into three main categories: (i) the upstream mechanism (Beresh *et al.* 2002; Ganapathisubramani *et al.* 2007, 2009; Vanstone & Clemens 2019); (ii) the downstream mechanism (Wu & Martin 2008; Piponniau *et al.* 2009; Priebe & Martín 2012; Ji *et al.* 2025); (iii) the combined effects of both upstream and downstream mechanisms (Souverein *et al.* 2010; Clemens & Narayanaswamy 2014; Martin *et al.* 2016). Ganapathisubramani *et al.* (2007, 2009) conducted numerical simulations and experimental research, and concluded that the superstructures in the turbulent boundary layer, which are 30–40 times the thickness of the boundary layer, are the main cause of low-frequency oscillations, i.e. the upstream mechanism. Priebe & Martín (2012) found that the unsteady motion of the shock wave is related to the 'breathing' of the separation bubble and the oscillation of the shear layer, but has a very weak correlation with the upstream boundary layer, which provides evidence for the downstream mechanism. In addition, Martin *et al.* (2016) found that the Görtler vortices are modulated by the disturbances in the upstream boundary layer, and in turn affect the unsteady characteristics of the separated flow, ultimately leading to the simultaneous operation of the upstream/downstream mechanisms in the low-frequency oscillation of the STBLI. Besides the low-frequency motions, the amplification of the pressure fluctuations is another important characteristic of STBLI. Bernardini *et al.* (2011) observed that in STBLI, the intensity of wall pressure fluctuations remains nearly constant upstream of the interaction region, but is significantly amplified downstream (Fang *et al.* 2020; Tong *et al.* 2021; Zhong *et al.* 2021; Bernardini *et al.* 2023; Ceci *et al.* 2024). Fang *et al.* (2020) studied the phenomenon of the turbulence amplification in STBLI, and discovered that the pressure fluctuations were mainly amplified within the low-frequency range during the initial amplification of turbulence, while the mid-frequency components gained more energy after the detachment of the shear layer. Hirai & Kawai (2023) compared the results of different wall temperatures, and found that wall cooling not only enhanced the low-frequency components of the wall pressure fluctuations, but strengthened the high-frequency components as well. Laguarda *et al.* (2024*b*) found that near the separation shock foot, the wall pressure exhibits a moderate low-frequency component at low Reynolds numbers, while at high Reynolds numbers, strong intermittency can be observed. Based on frequency–wavenumber spectra of the wall pressure fluctuations downstream of the interaction region, Cai *et al.* (2022) identified two distinct modes characterised by different convective velocities.

Due to the requirements of lightweight designs, the structures of aircraft are more susceptible to deformation and even vibration, resulting in a more significant coupling interaction between fluid and structure. Nevertheless, it is noteworthy that the majority of studies on STBLI focus on rigid geometric structures, with only incremental progress achieved in this field in recent years. Accordingly, the investigations into STBLI over

https://doi.org/10.1017/jfm.2026.12068 Published online by Cambridge University Press

a flexible panel have gradually gained traction, as such configurations better reflect realistic engineering geometries. Currently, relatively few studies have focused on panel vibration or flexible panels. On the experimental side, Spottswood *et al.* (2012) employed both surface pressure measurements and digital image correlation techniques to capture the vibration response of a fixed elastic panel in STBLI. Their findings revealed that the panel's response contains low-frequency components and is highly sensitive to the shock impingement location. Acosta & Austin (2024) measured the full-field surface deformations of the compliant panel via a single camera photogrammetry system in the experiment at Mach 4. Modal analysis of the surface deformation revealed that the first vibration mode of the panel is dominant in the panel response, and the first four vibration modes account for more than 98 % of the panel's vibration energy. Varigonda & Narayanaswamy (2023) measured wall pressure fluctuations in the experiment at Mach 2.5, and found that the low-frequency unsteadiness of the shock wave is amplified over the flexible panel. This phenomenon was also observed by Tripathi *et al.* (2023) in experiments with varying cavity pressures. On the numerical side, Visbal (2014) conducted a systematic investigation into the flutter characteristics of panels subjected to oblique shock impingement by coupling the inviscid/viscous fluid flows with the nonlinear von Karman plate theory. Building on this work, Boyer *et al.* (2018, 2021) extended the study to three-dimensional inviscid flows. Shinde *et al.* (2019) further extended the research to shock wave/transitional boundary layer interaction over flexible panels. Moreover, Shinde *et al.* (2022) investigated the fluid–structure interaction between a flexible panel and STBLI at Mach 4. The study revealed that the large deflections of the panel induced by STBLI lead to structural nonlinearity, which is manifested as coupling between bending and stretching of the panel. Laguarda *et al.* (2024*a*) investigated the dynamic coupling between STBLI and a flexible panel at Mach 2, and found that low-frequency modes unrelated to fluid–structure coupling qualitatively resembled those observed in a rigid panel, suggesting that the low-frequency unsteadiness of STBLI coexists with dynamics induced by fluid–structure interaction. Furthermore, Laguarda *et al.* (2024*a*) also found that the mean separation bubble is highly sensitive to mean surface deformations, whereas the influence of dynamic panel motion around the mean deflection can be almost negligible. Kimmel *et al.* (2025) numerically simulated the configuration where an elastic panel is located downstream of a compression ramp, and argued that one-way coupling exists between turbulence and structural responses: structural deformations significantly affect turbulence properties, while variations in turbulence have minor effects on structural responses.

The literature survey above shows that current research on the coupling between STBLI and structural vibrations primarily focuses on the vibrational characteristics of the wall panels in such flows, whereas studies regarding how panel vibration alters STBLI flow properties are still limited. Although prior studies (Shinde *et al.* 2022; Laguarda *et al.* 2024*a*) have confirmed the amplification of low-frequency unsteadiness induced by panel vibration, the fundamental physical mechanism behind this phenomenon has not been elucidated. Considering the complexity of such a flow phenomenon, it is probably more prudent to consider the flow over a panel with a given vibration mode before the feedback to the structural dynamics is incorporated. This serves as the motivation of the present study. We conduct direct numerical simulations (DNS) of STBLI flows over a vibrating panel with two commonly encountered low-order vibration modes, and focus on investigating the impact and inherent physical mechanism of the wall panel vibration on the low-frequency unsteady characteristics of the flow separation zone and wall pressure fluctuations.

https://doi.org/10.1017/jfm.2026.12068 Published online by Cambridge University Press

Ma	Re	T_∞	T_w	β_s
2.9	5.6×10^6 m^{-1}	108.1 K	307.0 K	30°

Table 1. Computational inflow parameters.

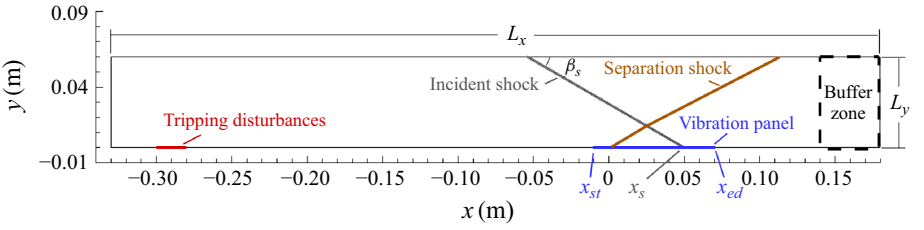


Figure 1. Sketch of the computational domain.

The rest of the paper is organised as follows. Section 2 presents the numerical simulation set-up and the validation of the results. Subsection 3.1 compares the effects of vibrating panels on the wall mean flow quantities and pressure fluctuations. In § 3.2, phase averaging is adopted to analyse the variations of wall pressure and separation bubble motion with panel vibration. Two-point correlation is utilised in § 3.3 to investigate the propagation characteristics of wall pressure fluctuations. Finally, § 3.4 employs dynamic mode decomposition to analyse the evolution of pressure fluctuations and flow structures under panel vibration. Section 4 summarises the key findings of the paper.

2. Numerical methods and validation

2.1. *Computation model*

This study investigates a supersonic turbulent boundary layer with free-stream Mach number $Ma = 2.9$ and unit Reynolds number $Re = 5.6 \times 10^6$ m^{-1}. The computational inflow parameters are summarised in table 1. The free-stream temperature T_∞ and wall temperature T_w are 108.1 and 307.0 K, respectively. As illustrated in figure 1, an incident shock wave with shock angle $\beta_s = 30°$ is introduced by enforcing the Rankine–Hugoniot conditions at the upper domain boundary, inducing flow deflection 12°. In the figure, x_s refers to the theoretical shock impingement location, with value 0.05 m.

The length of the computational domain L_x is set as $0.51L_{ref}$ (where $L_{ref} = 1$ m is the unit length), and the height L_y and width L_z are set as $0.06L_{ref}$ and $0.014L_{ref}$, respectively. The domain is discretised using $1401 \times 201 \times 141$ grid points in the streamwise (x), wall-normal (y) and spanwise directions (z). The mesh is uniformly distributed in the spanwise direction, and stretched in the streamwise and wall-normal directions to resolve fine-scale structures near the shock foot (denoted x_s in figure 1) and the wall. The grid intervals near the foot of the incident shock wave are $\Delta x^+ \approx 8.83$ in the streamwise direction, $\Delta y_w^+ \approx 0.44$ in the normal direction at the wall, $\Delta y_\delta^+ \approx 6.49$ at the outer edge of the boundary layer, and $\Delta z^+ \approx 4.42$ in the spanwise direction. The viscous scales are taken at a reference station $x = -0.024L_{ref}$.

The steady laminar profiles of velocity, density and temperature are imposed at the inlet boundary. Periodic conditions are adopted in the spanwise direction. The supersonic outlet condition is enforced at the outlet boundary with a streamwise grid gradual

https://doi.org/10.1017/jfm.2026.12068 Published online by Cambridge University Press

coarsening region (namely the buffer zone) to suppress spurious numerical reflections. The buffer zone covers the streamwise range $x = (0.14{-}0.18)\ L_{ref}$. The isothermal no-slip and no-penetration conditions are applied at the wall. A band of tripping disturbances (Cai *et al.* 2022) is introduced within the region $-0.3L_{ref} \le x \le -0.28L_{ref}$ to trigger bypass transition. The disturbances adopt the form of Pirozzoli *et al.* (2004), i.e.

$$v(x, z, t) = A_{amp}\ f(x)\ g(z)\ h(t), \quad x_a \le x \le x_b, \tag{2.1}$$

where A_{amp} is set to 0.2, and $[x_a, x_b]$ indicates the streamwise range of the disturbances. The form of $f(x)$ is given as

$$\begin{aligned} f(x) &= 4 \sin\theta\ (1 - \cos\theta)/\sqrt{27}, \\ \theta &= 2\pi\ (x - x_a)\ /\ (x_b - x_a)\ . \end{aligned} \tag{2.2}$$

However, the forms of $g(z)$ and $h(t)$ are different from those of Pirozzoli *et al.* (2004), i.e.

$$g(z) = \cos\left(2\pi\omega_z z/L_z\right), \tag{2.3}$$

$$h(t) = 1, \tag{2.3}$$

where ω_z is set to 4, and L_z denotes the spanwise width of the computational domain. Furthermore, these disturbances are imposed throughout the entire numerical simulation.

The streamwise extent of the vibration panel is defined by $x_{st} = -0.0109L_{ref}$ and $x_{ed} = 0.0704L_{ref}$. Similarly, the spanwise extent is defined by $z_{st} = 0.0005L_{ref}$ and $z_{ed} = 0.0135L_{ref}$, which is slightly narrower than the spanwise width of the computational domain. The vibration panel region is highlighted by the blue solid line in figure 1. The instantaneous position y_w of wall grid points of the vibrating panel can be expressed as

$$y_w = A \sin\left(\frac{2\pi}{T_p}t\right) \sin\left(\frac{m\pi\ (x - x_{st})}{a}\right) \sin\left(\frac{n\pi\ (z - z_{st})}{b}\right), \tag{2.4}$$

where A is the vibration amplitude of the wall panel, given as $0.001L_{ref}$ ($A/\delta \approx 0.157$, and δ is the nominal boundary layer at the reference station, as will be given later), which approximates the maximum deflection of flexible panels reported in Shinde *et al.* (2022) and Laguarda *et al.* (2024*a*). The vibration period $T_p \approx 185.67\delta/U_\infty$ is close to the period of the low-frequency motion in the rigid wall. Parameters a and b denote the panel length and width, respectively. Here, m and n represent the streamwise and spanwise mode numbers, respectively, which determine the vibration pattern.

Two vibration modes are considered in present simulations, i.e. vibration mode (1, 1) with $m = 1,\ n = 1$, and vibration mode (2, 1) with $m = 2,\ n = 1$, as prior literature (Shinde *et al.* 2022; Laguarda *et al.* 2024*a*; Tripathi *et al.* 2024) has demonstrated that these two modes dominate the vibrational response of a flexible panel under STBLI aerodynamic loading. For comparison, a rigid wall case was employed as the baseline. Hereinafter, we will refer to the case with a rigid wall as case R, and the vibration panel cases with vibration mode (1, 1) and mode (2, 1) as cases VM11 and VM21, respectively (Tripathi *et al.* 2023).

2.2. *Governing equations and numerical method*

The conservative forms of compressible Navier–Stokes equations in curvilinear coordinates are written as

$$\frac{\partial \widehat{Q}}{\partial t} + \frac{\partial \widehat{F}_c}{\partial \xi} + \frac{\partial \widehat{G}_c}{\partial \eta} + \frac{\partial \widehat{H}_c}{\partial \zeta} - \left(\frac{\partial \widehat{F}_v}{\partial \xi} + \frac{\partial \widehat{G}_v}{\partial \eta} + \frac{\partial \widehat{H}_v}{\partial \zeta}\right) = 0, \tag{2.5}$$

https://doi.org/10.1017/jfm.2026.12068 Published online by Cambridge University Press

where $\widehat{Q} = (1/J)\{\rho, \rho u, \rho v, \rho w, \rho e\}$ denotes the conservative vector, $(\widehat{F}_c, \widehat{G}_c, \widehat{H}_c)$ represents the inviscid flux in the computational coordinates (ξ, η, ζ), respectively, and $(\widehat{F}_v, \widehat{G}_v, \widehat{H}_v)$ denotes the viscous flux in the corresponding directions. The forms of the flux terms $\widehat{F}_c$ and $\widehat{F}_v$ are

$$\widehat{F}_c = \frac{1}{J}\begin{bmatrix} \rho U \\ \rho u U + p\xi_x \\ \rho v U + p\xi_y \\ \rho w U + p\xi_z \\ (\rho e + p)\, U - p\xi_t \end{bmatrix}, \quad \widehat{F}_v = \frac{1}{J}\begin{bmatrix} 0 \\ \xi_x\tau_{xx} + \xi_y\tau_{xy} + \xi_z\tau_{xz} \\ \xi_x\tau_{xy} + \xi_y\tau_{yy} + \xi_z\tau_{yz} \\ \xi_x\tau_{xz} + \xi_y\tau_{yz} + \xi_z\tau_{zz} \\ \xi_x b_x + \xi_y b_y + \xi_z b_z \end{bmatrix}, \tag{2.6}$$

where

$$\begin{cases} U = \xi_x u + \xi_y v + \xi_z w + \xi_t, \\ V = \eta_x u + \eta_y v + \eta_z w + \eta_t, \\ W = \zeta_x u + \zeta_y v + \zeta_z w + \zeta_t, \end{cases} \quad \begin{cases} b_x = -q_x + u\tau_{xx} + v\tau_{xy} + w\tau_{xz}, \\ b_y = -q_y + u\tau_{xy} + v\tau_{yy} + w\tau_{yz}, \\ b_z = -q_z + u\tau_{xz} + v\tau_{yz} + w\tau_{zz}. \end{cases} \tag{2.7}$$

The flux terms $\widehat{G}_c$, $\widehat{G}_v$, $\widehat{H}_c$, $\widehat{H}_v$ have similar forms, so they are not given here for brevity. Herein, (u, v, w) represents the velocity components of the streamwise, wall-normal and spanwise directions, respectively. Here, ρ, p and e are the density, pressure, and total energy per volume, respectively. The viscous stress τ_{ij} and heat flux q_i ($i, j = 1, 2, 3$, also as x, y and z) are determined by the constitutive equation of Newtonian gas and Fourier's law,

$$\tau_{ij} = \mu\left(\frac{\partial u_i}{\partial x_j} + \frac{\partial u_j}{\partial x_i}\right) - \frac{2}{3}\mu\frac{\partial u_k}{\partial x_k}\delta_{ij}, \quad q_j = -\kappa\frac{\partial T}{\partial x_j}, \tag{2.8}$$

with the viscosity coefficient μ determined by the Sutherland's law. The heat conductivity κ is calculated by the formula

$$\kappa = \frac{\mu c_p}{Pr}, \tag{2.9}$$

where Pr is the Prandtl number, and c_p is specific heat at constant pressure. Furthermore, $(\xi_x, \xi_y, \xi_z, \eta_x, \eta_y, \eta_z, \zeta_x, \zeta_y, \zeta_z)$ represent the metrics transforming Cartesian coordinates (x, y, z, t) into computational coordinates (ξ, η, ζ, t). The Jacobian determinant J is defined as

$$J = \begin{vmatrix} \xi_x & \xi_y & \xi_z & \xi_t \\ \eta_x & \eta_y & \eta_z & \eta_t \\ \zeta_x & \zeta_y & \zeta_z & \zeta_t \\ 0 & 0 & 0 & 1 \end{vmatrix}, \tag{2.10}$$

representing the reciprocal of the volume of the grid cell. Here, (U, V, W) are the contravariant velocities, denoting the projection of the velocity in the Cartesian coordinates onto the computational coordinates.

The governing equations are solved using an in-house code for DNS. The inviscid flux terms are discretised by a seventh-order weighted compact nonlinear scheme (Deng & Zhang 2000) in the smooth regions, and the monotone upstream-centred scheme for conservation laws in the flow discontinuities detected by a modified Ducros shock detector (Sciacovelli *et al.* 2021). The viscous fluxes are computed using an eighth-order

https://doi.org/10.1017/jfm.2026.12068 Published online by Cambridge University Press

central-difference scheme. Time advancement is achieved with a third-order TVD Runge–Kutta method (Gottlieb & Shu 1998).

The time advancement should be carefully treated due to the time-variant deformed grid distributions. Equation (2.5) can be simplified as

$$\frac{\partial \widehat{Q}}{\partial t} = R(Q) \quad \Rightarrow \quad \frac{1}{J}\frac{\partial Q}{\partial t} + Q\frac{\partial}{\partial t}\left(\frac{1}{J}\right) = R(Q), \tag{2.11}$$

where $Q = \{\rho, \rho u, \rho v, \rho w, \rho e\}$. Due to grid deformation, the time derivative of $1/J$ is not zero. In order to maintain the original form of the Runge–Kutta method, (2.11) is reformulated as

$$\frac{1}{J}\frac{\partial Q}{\partial t} = R(Q) - Q\frac{\partial}{\partial t}\left(\frac{1}{J}\right). \tag{2.12}$$

Therefore, the third-order TVD Runge–Kutta method can be specifically expressed as

$$\begin{aligned}
Q^{(0)} &= Q^n, \\
Q^{(1)} &= Q^{(0)} + J^{n+1}\,\Delta t\left[R\big(Q^{(0)}\big) - Q^{(0)}\frac{\partial}{\partial t}\left(\frac{1}{J}\right)^{n+1}\right], \\
Q^{(2)} &= \frac{3}{4}Q^{(0)} + \frac{1}{4}Q^{(1)} + \frac{1}{4}J^{n+1}\,\Delta t\left[R\big(Q^{(0)}\big) - Q^{(1)}\frac{\partial}{\partial t}\left(\frac{1}{J}\right)^{n+1}\right], \\
Q^{(3)} &= \frac{1}{3}Q^{(0)} + \frac{2}{3}Q^{(2)} + \frac{2}{3}J^{n+1}\,\Delta t\left[R\big(Q^{(0)}\big) - Q^{(2)}\frac{\partial}{\partial t}\left(\frac{1}{J}\right)^{n+1}\right], \\
Q^{n+1} &= Q^{(3)},
\end{aligned} \tag{2.13}$$

where the superscript (i) $(i = 0, 1, 2, 3)$ indicates the ith Runge–Kutta sub-step, and Q^n, Q^{n+1} represent Q at times n and $n+1$, respectively. Moreover, J and $(\partial/\partial t)(1/J)$ at time step $n+1$ in (2.13) are calculated before the the time advancement, since grid deformation and the calculation of grid metrics precede the time advancement.

The grid metrics are calculated by the method proposed by Liao & Ye (2015) to meet the geometric conservation law for deformed grids. The grid deformation for the panel vibration is handled via the inverse distance weighting method, as follows:

$$\boldsymbol{S}_w(g_i) = \frac{\sum_{g_w \in \Omega_w}\left[\left(\dfrac{1}{|\Delta \boldsymbol{s}_w|}\right)^{a_c} \cdot \boldsymbol{S}_w(g_w)\right]}{\sum_{g_w \in \Omega_w}\left[\left(\dfrac{1}{|\Delta \boldsymbol{s}_w|}\right)^{a_c}\right]}, \tag{2.14}$$

where $\boldsymbol{S}_w$ is the displacement vector of grid points in Cartesian coordinates, g_i and g_w represents the inner and wall grid points, respectively, Ω_w is the collection of moving grid points on the wall, and $|\Delta \boldsymbol{s}_w|$ denotes the Euclidean distance between g_i and g_w prior to deformation. The artificial parameter a_c is set to 4 in this study, confining the grid deformation within $0.78L_y$ in the y direction.

2.3. *Validation*

The nomenclatures are first introduced here. For a generic flow quantity φ, its ensemble average is denoted by $\bar{\varphi}$, and the corresponding fluctuation is represented by φ'. The Favre average is denoted by $\tilde{\varphi}$, and the corresponding fluctuation is represented by φ''. The root mean square of the fluctuations is marked by the subscript rms.

https://doi.org/10.1017/jfm.2026.12068 Published online by Cambridge University Press

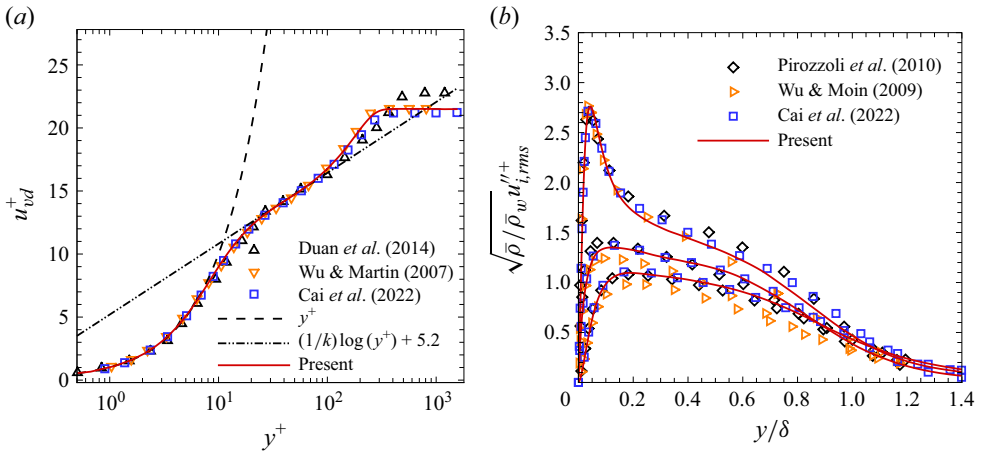


Figure 2. (*a*) The van-Driest-transformed mean velocity profile ($k = 0.41$). (*b*) The density-weighted turbulence intensities of velocity components plotted against the outer scales.

For turbulent statistics computation, approximately 10 000 flow samples are collected, with dimensionless sampling interval $0.00058L_{ref}/u_\infty$ and total duration $5.8L_{ref}/u_\infty$, covering approximately 5 periods of low-frequency pressure oscillations and wall vibrating periods.

As a validation of the DNS results, the basic statistics of the turbulent boundary layer at $x = -0.024L_{ref}$ are first reported, with nominal boundary layer thickness $\delta = 0.0064L_{ref}$, displacement thickness $\delta^* = 0.0020L_{ref}$, momentum thickness $\theta = 0.00049L_{ref}$, and friction Reynolds number $Re_\tau = 281.5$, defined as

$$Re_\tau = \frac{\rho_w u_\tau \delta}{\mu_w}, \tag{2.15}$$

where u_τ denotes the friction velocity, calculated as $\sqrt{\tau_w/\rho_w}$, with τ_w representing the wall shear stress. The variables normalised by these viscous scales are marked by the superscript '+'. Figure 2(*a*) presents the van-Driest-transformed mean velocity profile u_{vd} defined as

$$u_{vd} = \int_0^{\tilde{u}} \sqrt{\frac{\bar{\rho}}{\bar{\rho}_w}}\,\mathrm{d}\tilde{u}, \tag{2.16}$$

along with those reported by Wu & Martin (2007), Duan *et al.* (2014) and Cai *et al.* (2022). The present results conform to the linear law in the viscous sublayer and the logarithmic law in the logarithmic region, and show excellent agreement with reference results. Deviations observed in the wake region may be attributed to differences in Re_τ.

Figure 2(*b*) displays the density-weighted velocity fluctuation intensities, plotted using outer scaling y/δ. In the near-wall region, the u'' intensity peaks at $y/\delta \approx 0.043$ (or $y^+ \approx 12$) before decreasing monotonically. The v'' and w'' distributions exhibit profiles similar to u'', though with consistently lower magnitudes throughout the boundary layer. Numerical results from Wu & Moin (2009), Pirozzoli *et al.* (2010) and Cai *et al.* (2022) are reported for comparison, demonstrating good agreement with the results of the present study.

The root mean square of the pressure fluctuations normalised by the local wall shear stress is shown in figure 3. The pressure fluctuation intensity peaks at $y^+ \approx 24$, then decreases rapidly and maintains relatively low values in the wake region. The present

https://doi.org/10.1017/jfm.2026.12068 Published online by Cambridge University Press

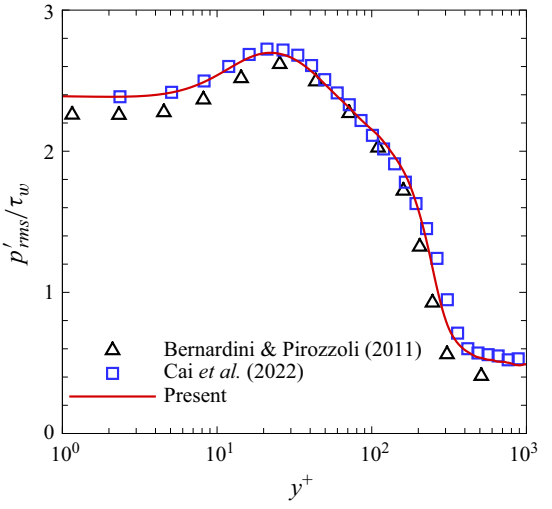


Figure 3. Root mean square of the pressure fluctuation plotted against the inner scales.

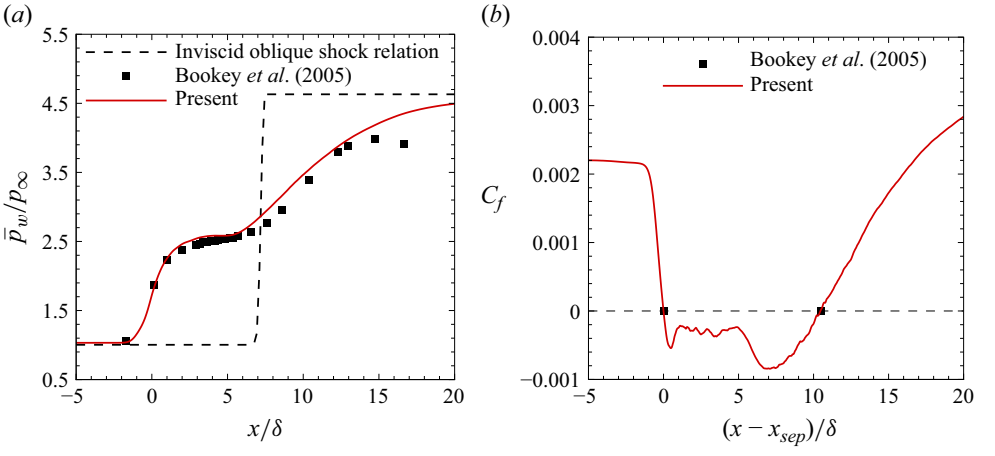


Figure 4. (*a*) Mean wall pressure and (*b*) mean skin-friction coefficient on the rigid wall.

results show good agreement with reference data (Bernardini & Pirozzoli 2011; Cai *et al.* 2022), although they are slightly higher than the results of Bernardini & Pirozzoli (2011) in the near-wall region. This discrepancy may be attributed to differences in the friction Reynolds numbers. The consistent statistical results with those of the previous studies suggest that the current DNS databases are valid, and the turbulent boundary layer is fully developed at the reference location.

In order to verify the reliability of the calculation for STBLI, the mean wall pressure and mean skin-friction coefficients for the rigid wall case are reported in figures 4(*a*) and 4(*b*), respectively. When impinged by a strong shock wave, the mean wall pressure experiences two stages of elevation, which is a typical feature of separated flow (Babinsky & Harvey 2011).The mean wall pressure in the present study collapses well with the experimental result of Bookey *et al.* (2005). In figure 4(*b*), the mean skin-friction coefficient of the incoming turbulent boundary layer is approximately 0.00218 and shows good agreement with the result of Bookey *et al.* (2005), which is approximately 0.00225. The mean separation and reattachment points are marked with the cross-zero points. The length of the

https://doi.org/10.1017/jfm.2026.12068 Published online by Cambridge University Press

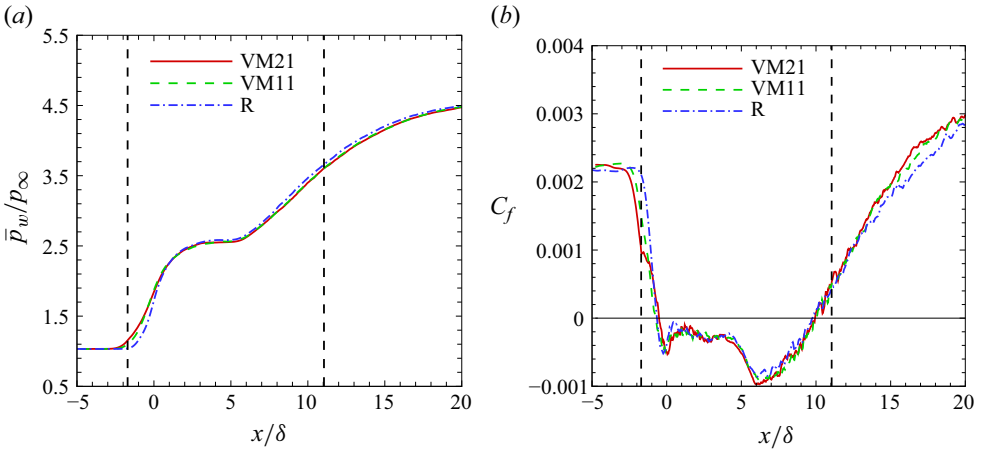


Figure 5. (*a*) Mean wall pressure and (*b*) mean skin-friction coefficient at the spanwise centre plane. The black dashed lines mark the front and rear edges of the wall panel.

mean separation bubble in the present study is also consistent with the experimental results (Bookey *et al.* 2005). These flow statistics further confirm the validity of the numerical methods and results adopted herein.

3. Results and discussion

3.1. *Mean flow and unsteady characteristics*

Figure 5 shows the distributions of the mean skin-friction coefficient C_f and mean wall pressure $\bar{p}_w/\bar{p}_\infty$ at the spanwise centre plane, to illustrate the influence of different vibration modes on the average flow field. The mean wall pressure distributions for the vibrating panel are in general similar to the rigid wall case. The difference lies in the upstream shift of the starting point of the mean pressure elevation. The abatement of the mean skin friction coefficients C_f in cases VM21 and VM11 also occurs at earlier positions, suggesting that flow separation is moving upstream in these cases. Downstream of the panel, the vibrating panels slightly increase the skin friction, which is probably caused by the stronger internal shear layer compared with case R.

Although the mean flow separation and the wall flow quantities are not much affected, the unsteady features, especially the low-frequency oscillations, are significantly modulated. In figure 6, we present the pre-multiplied frequency spectral density (PSD) of wall pressure fluctuations. For the rigid wall case R, a low-frequency wall pressure fluctuation signal in the vicinity of the mean separation point can be observed, with the frequencies $fL/U_\infty \approx 0.034-0.068$, where L is the separation length (i.e. $f\delta/U_\infty \approx 0.0033-0.0065$). The low-frequency band is broadly consistent with the prediction from Dussauge *et al.* (2006), Wu & Martin (2007), Priebe *et al.* (2009) and Laguarda *et al.* (2024*b*). For the vibrating panel cases VM11 and VM21, the low-frequency signal near the mean separation point is greatly enhanced in both magnitudes and the streamwise range. Intriguingly, in these vibrating panel cases, a new highly intensified low-frequency oscillation region can be observed within the interaction zone, with the characteristic frequencies identical to that of the panel vibration. The magnitudes of the high-intensity low-frequency oscillation gradually decay downstream, with those in case VM21 more rapidly than those in case VM11, the latter of which extends even beyond the flow reattachment point and is retained for a rather long distance downstream.

https://doi.org/10.1017/jfm.2026.12068 Published online by Cambridge University Press

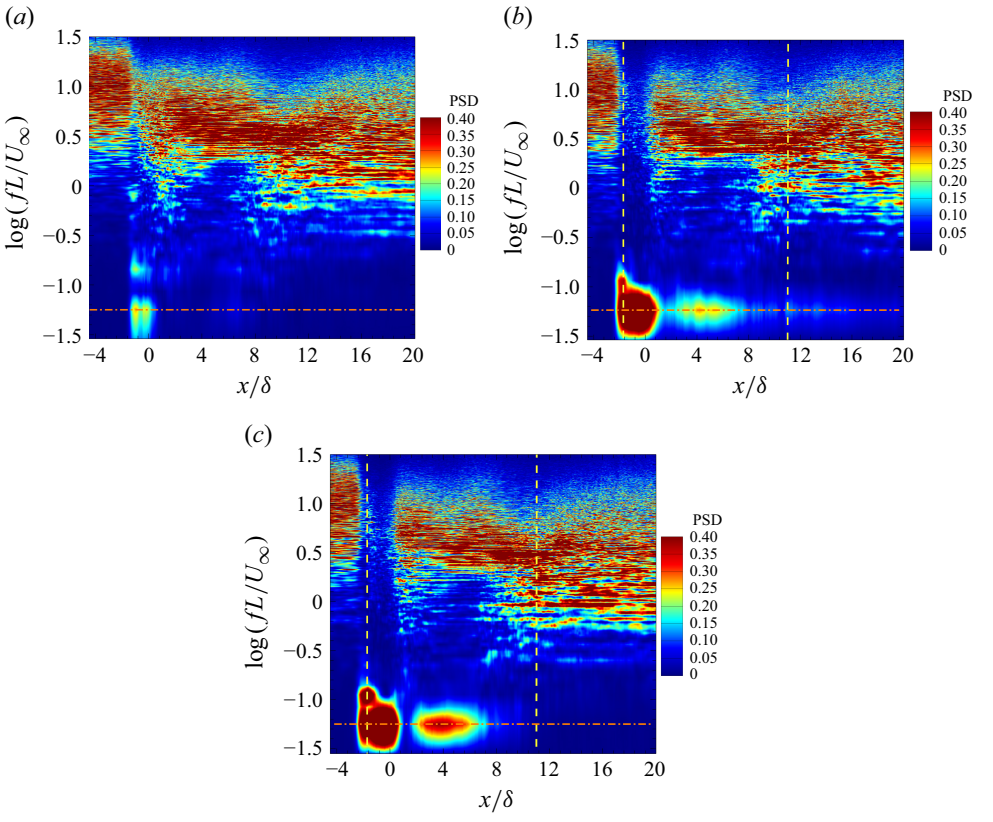


Figure 6. Pre-multiplied wall pressure frequency spectra of (*a*) case R, (*b*) case VM11 and (*c*) case VM21. The yellow dashed lines indicate the range of the panel vibration. Orange dash-dotted lines denote the wall panel vibration frequency.

Figure 7 presents space–time variations of wall pressure fluctuations along the spanwise centre plane, superimposed with contours of wall panel deflection to illustrate the coupled spatiotemporal evolution of panel vibration. Upon activation of the vibrating panel, a quasi-periodic signal emerges near the mean separation point, accompanied by similar features in the interaction zone. This is consistent with the newly identified low-frequency components in the frequency spectral density in figure 6. Notably, the low-frequency fluctuations near the mid-region of the panel and those around the mean separation point exhibit a distinct lack of synchronisation. Specifically, for case VM21 with the vibration mode (2, 1), a temporal delay of approximately half a period is observed between these signals, whereas for case VM11 with the vibration mode (1, 1), the mid-panel signal lags by approximately a quarter period. By correlating pressure fluctuations with panel deformation, a clear physical relationship can be established. When the first half of the panel with vibration mode (2, 1), or the entire panel with vibration mode (1, 1), bulges into the flow, positive pressure fluctuations arise near the mid-region, and vice versa. This indicates that the local pressure field in this region is governed by the instantaneous geometry of the vibrating panel. More importantly, a significant modal-dependent behaviour is identified. As the panel protrudes into the flow, the pressure fluctuations near the mean separation point remain predominantly negative in case VM21. In contrast, for case VM11, the pressure fluctuations turn negative specifically during the transition from maximum bulging to maximum bowing. These findings reveal that panel

https://doi.org/10.1017/jfm.2026.12068 Published online by Cambridge University Press

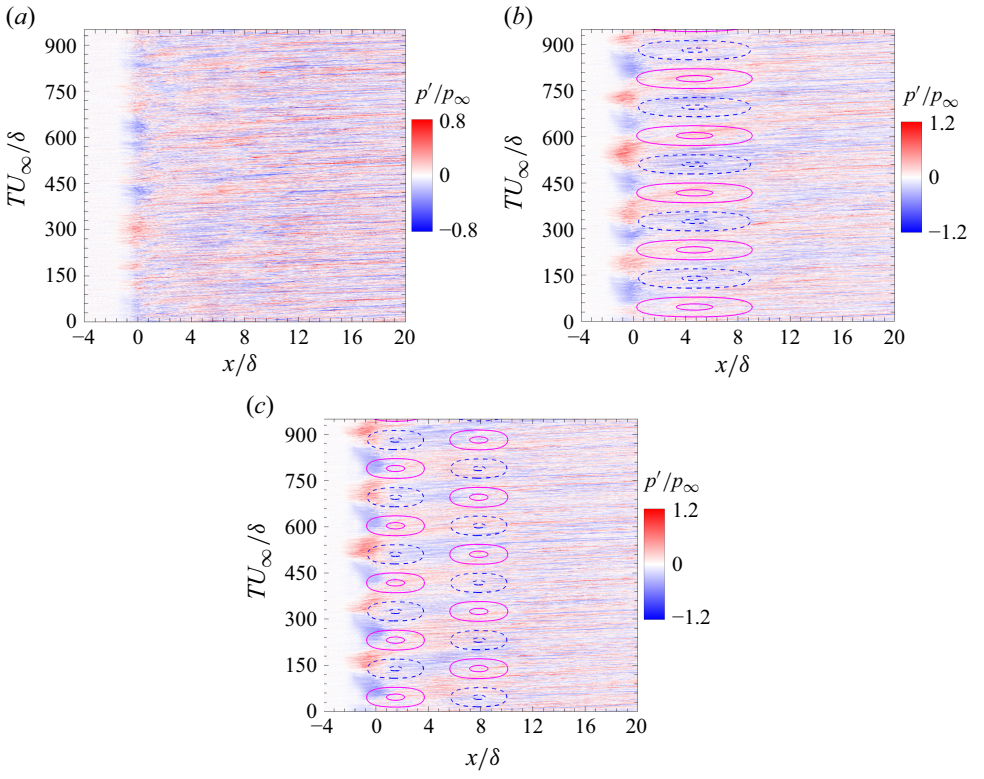


Figure 7. Space–time variations of wall pressure fluctuation along the streamwise centreline for (*a*) case R, (*b*) case VM11 and (*c*) case VM21. Panel deflection (as y_w/δ) is indcated as pink solid lines for positive, blue dashed lines for negative. Contour levels are −0.15 to 0.15, with increment 0.075.

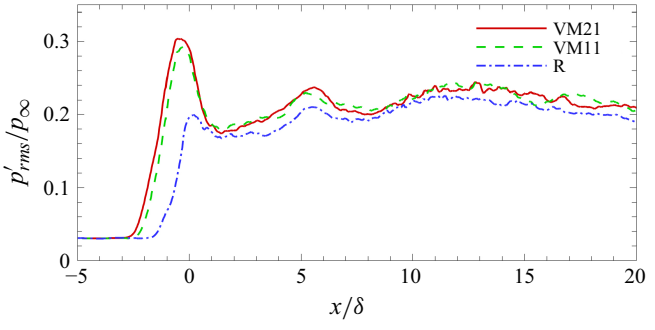


Figure 8. Variance of wall pressure along the streamwise direction.

vibration exerts a direct modulation on the pressure fluctuations in the separation region, yet underlying flow mechanisms are distinct across different vibrational modes.

Figure 8 presents the variance of wall pressure along the streamwise direction for different vibration modes. It can be clearly observed that panel vibration substantially amplifies the intensity of wall pressure fluctuations near the separation point. Further downstream, the fluctuation intensity decays rapidly and remains slightly higher than that of the rigid wall. However, different vibration modes have minor effects on the streamwise development of pressure fluctuation intensity.

https://doi.org/10.1017/jfm.2026.12068 Published online by Cambridge University Press

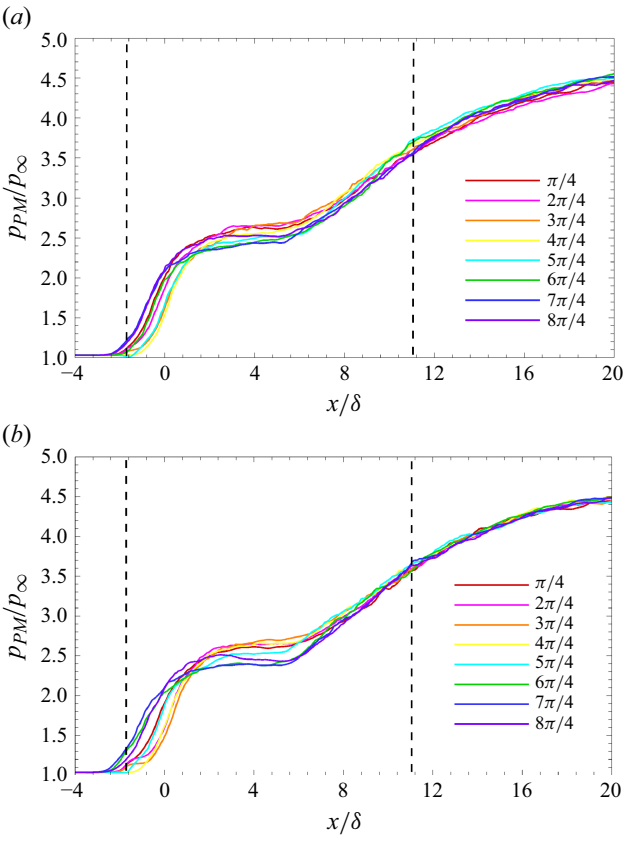


Figure 9. Phase-averaged wall pressure at eight phases ($\pi/4$, $2\pi/4$, $3\pi/4$, $4\pi/4$, $5\pi/4$, $6\pi/4$, $7\pi/4$, $8\pi/4$) in (*a*) case VM11 and (*b*) case VM21. Black dashed lines mark the range of the panel vibration.

3.2. *Mean flow variation with panel vibration – phase average*

Periodic panel vibrations with the frequency significantly lower than turbulent fluctuations allow the utilisation of phase averaging of the flow field. Since the vibration follows a sinusoidal temporal distribution, we select eight representative phases (denoted as χ) ranging from $\pi/4$ to 2π, with increment $\pi/4$, for detailed examination. The phase-averaged flow quantities are marked by the subscript 'PM'.

Figure 9 presents the phase-averaged wall pressure distribution at the spanwise centre plane. A key finding is the phase-dependent shift in the location of the initial pressure increment. As phase χ increases from $\pi/4$ to π, this location moves progressively downstream. Conversely, as χ continues to increase to 2π, it shifts upstream. This behaviour indicates that the protrusion of the front portion of the wall panel into the flow displaces the separation shock wave downstream, while its inward bending induces an upstream motion of the shock. This phenomenon is consistent with the observations reported by Zhang *et al.* (2014). These results clearly demonstrate that the separated shock wave position is actively modulated by the panel vibration, producing a distinct pressure signature near the mean separation location. Furthermore, in the mid-region of the wall panel where new low-frequency signals emerge, the wall pressure exhibits synchronous periodic variation with phase χ. As illustrated in figure 9, the pressure in this region increases when the panel protrudes into the flow, and decreases when it sags inwards,

https://doi.org/10.1017/jfm.2026.12068 Published online by Cambridge University Press

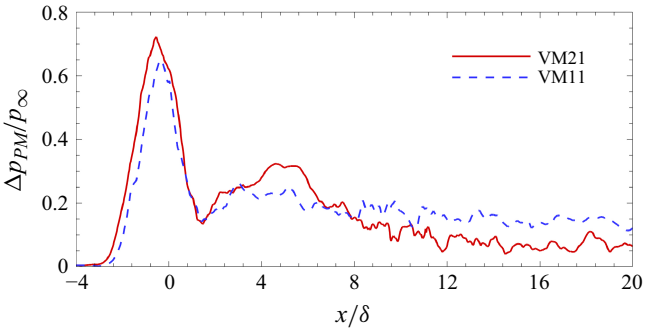


Figure 10. Streamwise distribution of mean pressure difference Δp_{PM} at the spanwise centre plane.

highlighting a strong local correlation between panel motion and the unsteady pressure field.

To highlight the wall pressure variation induced by panel vibration, we define the mean pressure difference

$$\Delta p_{PM} = p_{PM,max} - p_{PM,min}, \tag{3.1}$$

where $p_{PM,max}$ and $p_{PM,min}$ are the maximum and minimum values amongst these eight phase-averaged wall pressures, respectively. The results are shown in figure 10. The Δp_{PM} value exhibits a rapid amplification near the mean separation point, revealing substantial low-frequency fluctuations in this region, which is consistent with the elevated energy content in low-frequency signals shown in figure 6. Notably, the amplitude of Δp_{PM} for case VM21 slightly exceeds that in case VM11, which can be attributed to the greater panel curvature induced by the vibration in the former. A secondary growth in Δp_{PM} is observed near the mid-region of the wall panel, with a growth rate far lower than the Δp_{PM} growth near the separation point. This weak secondary amplification corresponds to the emergence of new low-frequency components identified in the frequency spectra. In this region, case VM21 also shows moderately larger mean pressure difference. A key distinction between the two vibration modes emerges downstream of the panel. While the fluctuation in case VM21 with the vibration mode (2, 1) gradually decays, it persists at a substantial level in case VM11 with the vibration mode (1, 1), even at distance 10δ downstream. This indicates that the panel vibration mode critically influences the downstream sustainability of low-frequency fluctuations, with vibration mode (1, 1) exhibiting a more prolonged impact on the flow field.

The low-frequency oscillation of the wall pressure is known to be associated with the dynamics of separation bubble (Wu & Martin 2008; Piponniau *et al.* 2009; Priebe & Martín 2012). Figures 11 and 12 present the phase-averaged streamwise velocity contours for cases VM21 and VM11, respectively, with the separation bubble identified by the contour line of $u_{PM} = 0$. A stark difference is observed between these two cases with distinct vibration modes. For case VM21, the separation bubble experiences an obvious streamwise oscillation: it moves downstream as the front half of the panel bulges outwards (figure 11*b*), returns toward its initial position as the panel flattens (figure 11*d*), and continues upstream when the front half retracts inwards (figure 11*f*). In contrast, in case VM11, the mode (1, 1) vibration primarily modulates the volume of the bubble. The bubble contracts when the entire panel bulges into the flow, and expands when it concaves inwards (figure 12). These results demonstrate that the motion of the separation bubble is determined by the panel vibration, but its specific effect, whether inducing streamwise oscillation or volume change, is dependent on the spatial mode shape of the vibration.

https://doi.org/10.1017/jfm.2026.12068 Published online by Cambridge University Press

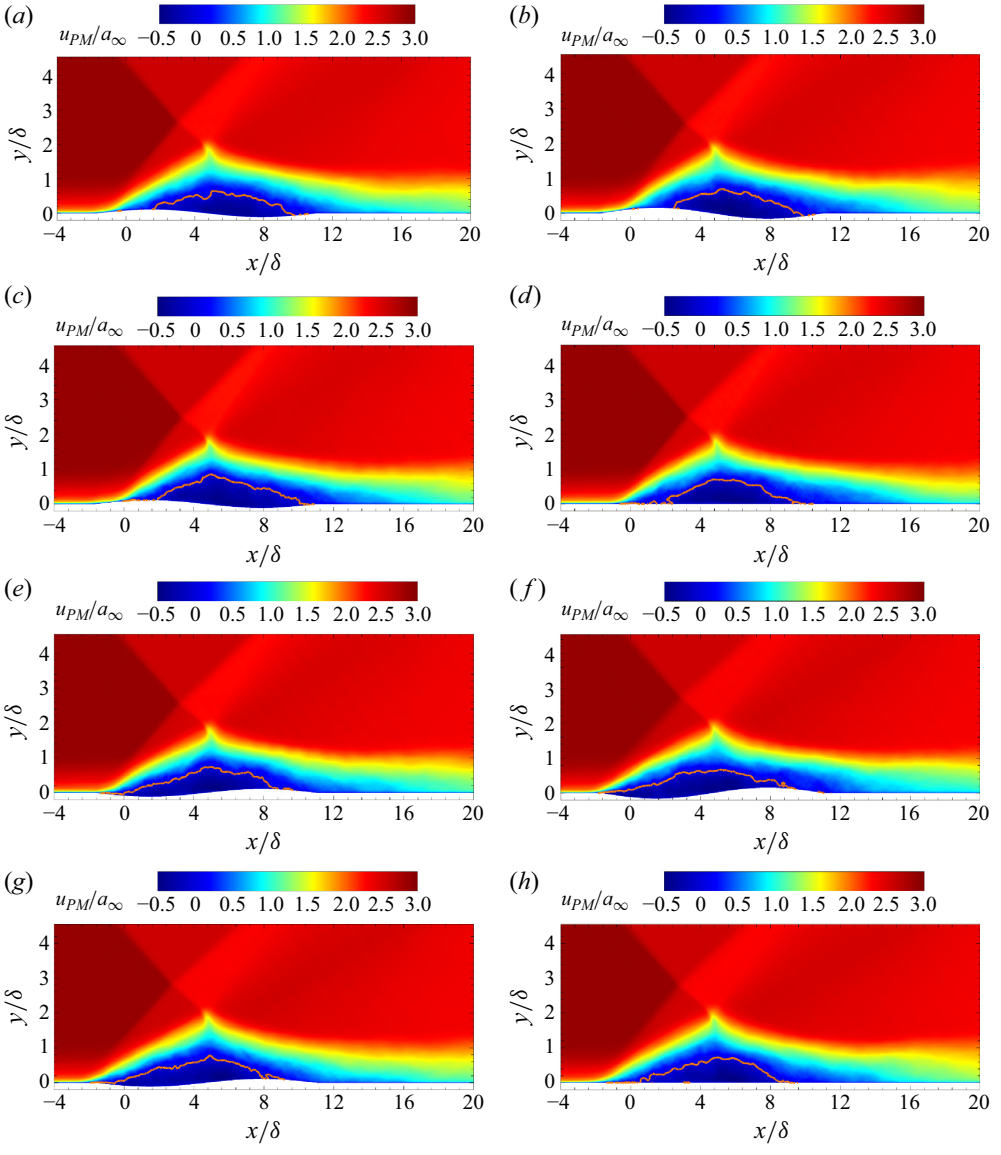


Figure 11. Phase-averaged streamwise velocity of case VM21 at phases (*a*) $\pi/4$, (*b*) $2\pi/4$, (*c*) $3\pi/4$, (*d*) $4\pi/4$, (*e*) $5\pi/4$, (*f*) $6\pi/4$, (*g*) $7\pi/4$ and (*h*) $8\pi/4$. Solid lines mark the separation bubble with $u_{PM} = 0$.

To quantitatively elucidate the distinct influence mechanisms of different vibration modes, we analyse the area of the separation bubble and streamwise centroid position across phases by statistically integrating the region where $u_{PM} < 0$, and calculating its area-weighted streamwise coordinate. Figure 13 presents these quantitative metrics. It should be noted that density weighting is not adopted in the present calculation of the streamwise centroid position, and even when density weighting is incorporated in the integration, the computed results exhibit no substantial discrepancy from those in figure 13. For case VM21 with the vibration mode (2, 1), the separation bubble undergoes a pronounced, coordinated streamwise oscillation. As the phase advances, the bubble initially moves downstream, reaching its farthest downstream position ($x/\delta \approx 6.1$)

https://doi.org/10.1017/jfm.2026.12068 Published online by Cambridge University Press

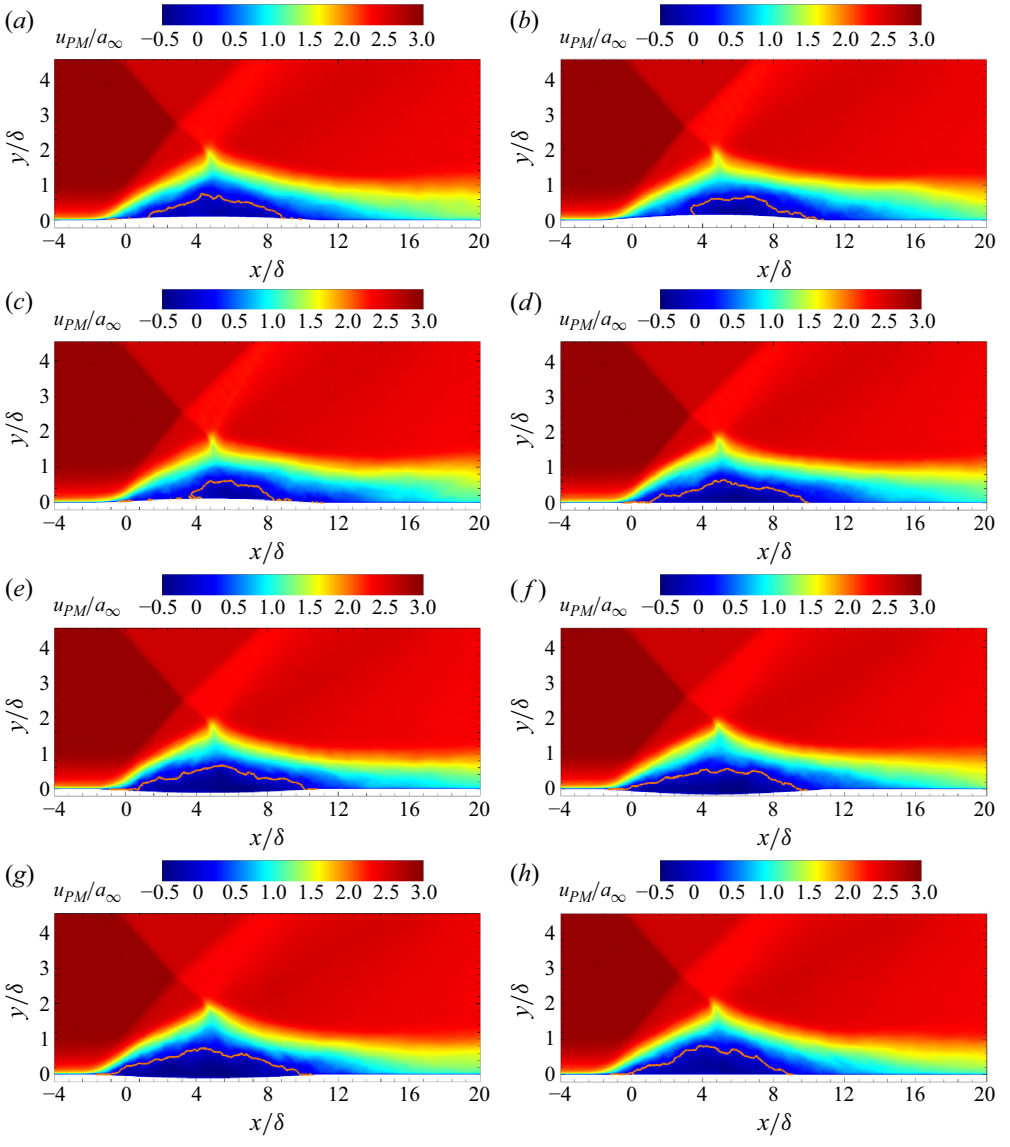


Figure 12. Phase-averaged streamwise velocity of case VM11 at phases (*a*) $\pi/4$, (*b*) $2\pi/4$, (*c*) $3\pi/4$, (*d*) $4\pi/4$, (*e*) $5\pi/4$, (*f*) $6\pi/4$, (*g*) $7\pi/4$ and (*h*) $8\pi/4$. Solid lines mark the separation bubble with $u_{PM} = 0$.

precisely when the front panel section is fully protruded. It then reverses direction, moving upstream as the phase continues to increase, and ultimately attains its most upstream position ($x/\delta \approx 3.8$) during the maximum inward bending of the front panel. The cycle completes as the panel flattens, with the bubble returning to the panel centre. Notably, throughout this entire reciprocating motion, the bubble area remains largely constant.

In contrast, the separation bubble for case VM11 with the vibration mode (1, 1) exhibits a different behaviour. Its streamwise centroid remains remarkably stable, anchored near the middle of the panel despite the panel vibration. The dominant response is instead a drastic, periodic variation in bubble volume. The area first contracts progressively with increasing phase, reaching its minimum value at phase $3\pi/4$. This is followed by a gradual expansion,

https://doi.org/10.1017/jfm.2026.12068 Published online by Cambridge University Press

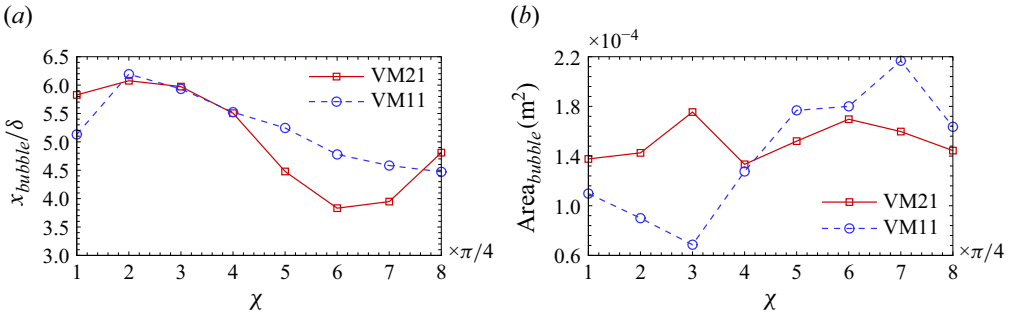


Figure 13. Streamwise position of (*a*) centroid and (*b*) area of the separation bubble at different phases in the spanwise centre plane.

with the bubble attaining its maximum volume at phase $7\pi/4$. The magnitude of this oscillation is substantial, with a variation range approximating 50 % of the time-averaged bubble area. From this quantitative trace, we can also identify a distinct phase lag. For case VM11, the variation of the bubble area lags the panel vibration by approximately $T_p/8$. This measured delay directly causes the generation of negative wall-pressure fluctuations near the separation point to lag behind the physical bulging of the wall panel in case VM11, as illustrated in figure 7.

The phase-averaged analyses confirm the observations in figures 11 and 12 that the spatial mode of vibration dictates the nature of the response of the separation bubble: panel vibration mode (2, 1) modulates its position via large-scale oscillating motions, while vibration mode (1, 1) governs its size via a potent breathing mode, with the phase lag being a critical component of the turbulence modulation in the latter.

3.3. *Propagation of low-frequency wall pressure*

We have identified in figure 6 that the low-frequency pressure fluctuations are capable of propagating through the interaction zone, reaching to a far position downstream. Such a propagation property can be evaluated by the spatiotemporal correlation between wall pressure fluctuations at a reference position x_{ref} and downstream,

$$C_{pp}(x,\,\Delta t) = \frac{\overline{p'\left(x_{ref},\,t\right)\,p'\left(x,\,t+\Delta t\right)}}{\left(\overline{p'^2\left(x_{ref},\,t\right)}\right)^{1/2}\left(\overline{p'^2\left(x,\,t+\Delta t\right)}\right)^{1/2}}. \tag{3.2}$$

Figure 14 shows the two-point spatiotemporal correlation of the wall pressure fluctuation with the reference position $x_{ref} = -3.6\delta$ located upstream of the interaction zone. Regardless of wall panel vibration modes, the two-point correlation results remain consistent. In all cases, the wall pressure fluctuations at the reference position exhibit positive correlation solely within a limited streamwise region. This correlation shows distinct inclination on the spatiotemporal correlation plane, indicating significant downstream pressure propagation. The convective velocity U_c from the spatiotemporal correlation can be defined as

$$U_c \equiv \frac{x_{Cpp,max} - x_{ref}}{\Delta t}, \tag{3.3}$$

where $x_{Cpp,max}$ is the streamwise location where the spatiotemporal correlation attains local maxima at the time delay Δt. Upstream of the interaction zone, U_c is approximately $0.63U_\infty$, similar to the results of Bernardini & Pirozzoli (2011), Duan *et al.* (2014) and Cai *et al.* (2022).

https://doi.org/10.1017/jfm.2026.12068 Published online by Cambridge University Press

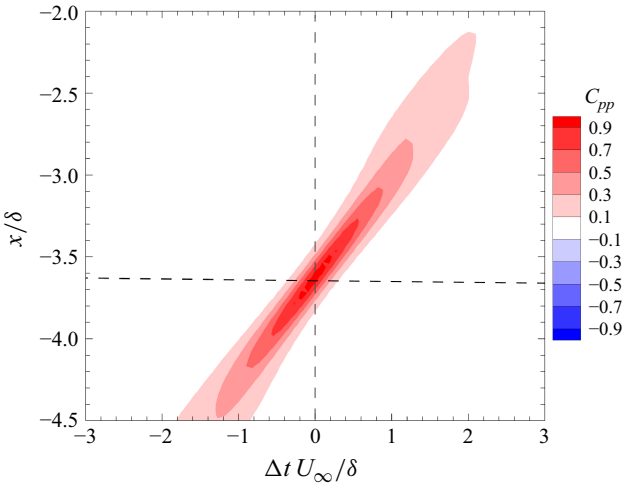


Figure 14. Distribution of the two-point spatiotemporal correlation of wall pressure fluctuations with $x_{ref} = -3.6\delta$. The black dashed lines mark the position of the reference point.

Figure 15 presents the two-point spatiotemporal correlation of wall pressure fluctuations with the reference position $x_{ref} = 4.0\delta$, situated near the mid-region of the wall panel. This analysis reveals how wall vibration reorganises the spatiotemporal coherence of the pressure field, in contrast to the baseline rigid wall case, whose spatiotemporal correlation resembles that of an upstream turbulent boundary layer, with only a weak negative correlation further downstream.

Under wall vibration, the spatiotemporal correlation becomes more complex. The significant correlations are primarily concentrated in two crucial regions: the mean separation point and the mid-region of the panel. We can find the emergence of a quasi-periodic alternation between positive and negative correlation values, observed both at the reference point itself (indicating modulated self-sustained oscillations) and, more importantly, in its relationship with the mean separation point. This suggests that the low-frequency pressure fluctuations in these two distinct regions are synchronised and share a common origin, namely the quasi-periodic oscillation imposed by the panel vibration.

A critical distinction between the vibration modes can be identified by the time delay associated with these correlations. For case VM21 with the vibration mode (2, 1), the positive correlation with the separation point occurs at time lag approximately $80\delta/U_\infty$ (approximately half a vibration period), indicating that a negative pressure fluctuation at the separation point occurs nearly in phase, with a positive fluctuation at the mid-region of the panel. In contrast, for the case VM11 with the vibration mode (1, 1), the corresponding time lag is only approximately $55\delta/U_\infty$ (approximately a quarter period), leading to an alternating phase relationship between the pressure fluctuations in the two regions. These elucidations are in agreement with the direct observations in figure 7. More significantly, they statistically validate that the pressure fluctuations in the mid-panel region and at the separation point are not independent, but are a coupled response to the panel vibration, thereby reinforcing the conclusion presented in § 3.2.

To investigate the spatiotemporal correlation of wall pressure fluctuations downstream of the interaction region, two-point correlations are computed with a reference point at $x_{ref} = 16.0\delta$, located 5δ downstream of the panel trailing edge. The spatiotemporal correlation contours and corresponding local zooming regions are presented in figure 16.

https://doi.org/10.1017/jfm.2026.12068 Published online by Cambridge University Press

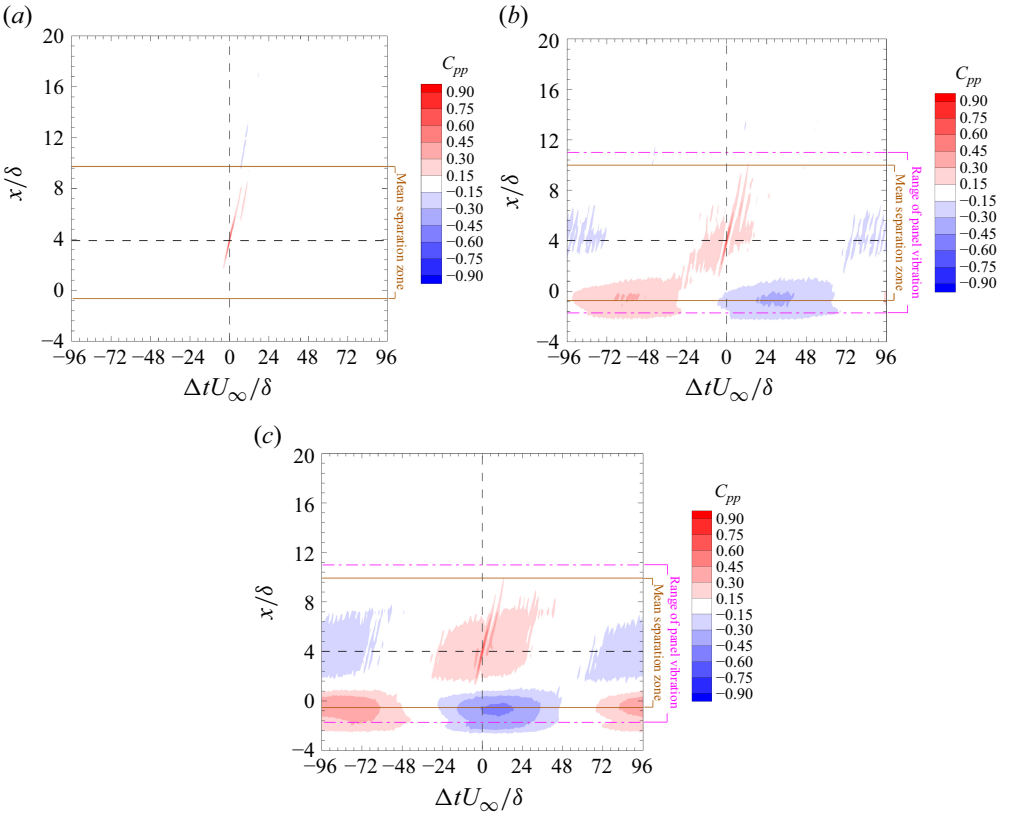


Figure 15. Distribution of the two-point spatiotemporal correlation of wall pressure fluctuations with $x_{ref} = 4.0\delta$ for (*a*) case R, (*b*) case VM11 and (*c*) case VM21. The black dashed lines mark the position of the reference point.

Since the local magnifications with different cases show nearly identical features, only the local magnification for case R is presented in the figure for brevity. In the rigid wall case R, the correlation pattern downstream of the panel exhibits a characteristic tilted 'X' shape, consistent with the coexistence of two distinct propagation modes of wall pressure fluctuations previously reported by Cai *et al.* (2022). The convection velocities corresponding to the two dash-dot-dotted lines in Figure16(*b*) are $0.505U_\infty$ and $0.968U_\infty$, respectively, which are also generally consistent with the results of Cai *et al.* (2022). When panel vibration is introduced, the overall structure of the spatial–temporal correlation remains qualitatively similar to the rigid wall baseline case for both vibration panel cases, suggesting that the propagation of wall pressure in this region is not significantly altered. The key modal-dependent distinction, however, emerges in the amplitude and distribution of the influence upstream. Specifically, in case VM11, a weakly correlated region persists in the vicinity of the mean separation point, as is visible in the view of figure 16(*c*). This sustained, albeit weak, correlation provides evidence that the low-frequency pressure signal observed far downstream in case VM11 originates from fluctuations generated near the separation zone. This finding indicates that the mode (1, 1) panel vibration facilitates a more effective upstream to downstream coupling of low-frequency disturbances, a behaviour not prominently observed in the mode (2, 1) panel vibration or rigid wall case. Henceforth, we can conclude that although the vibration

https://doi.org/10.1017/jfm.2026.12068 Published online by Cambridge University Press

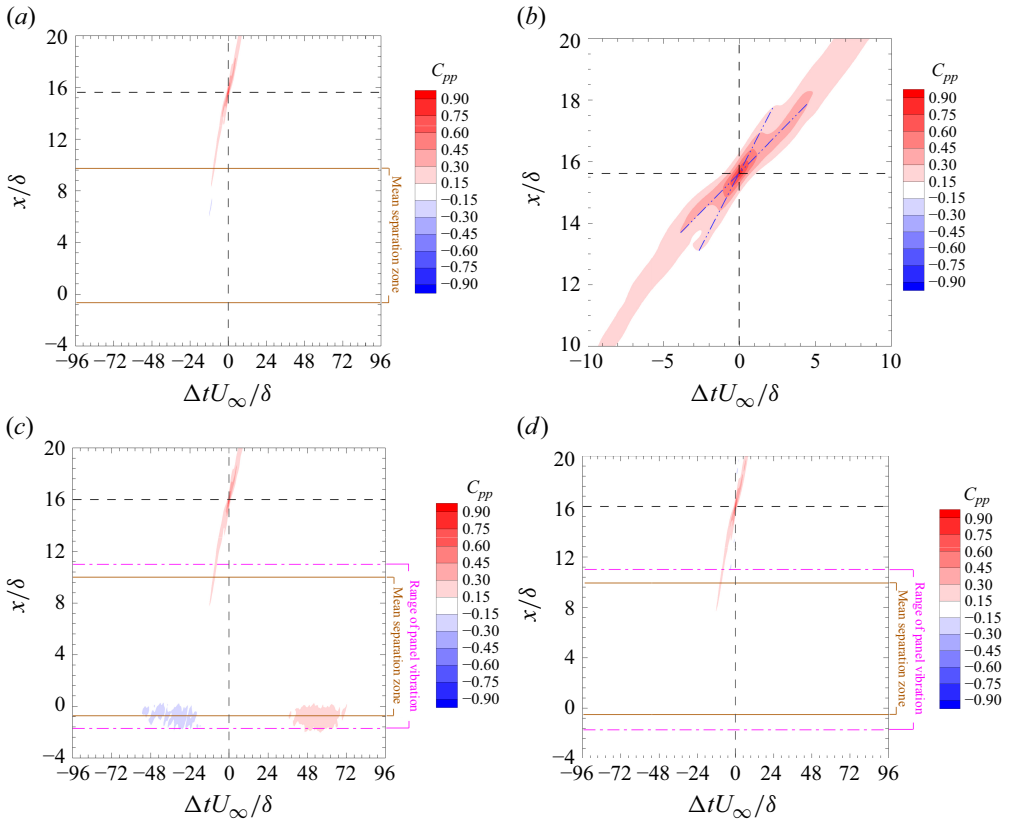


Figure 16. Distribution of the two-point spatiotemporal correlation of wall pressure fluctuations with $x_{ref} = 16.0\delta$ for (*a*) case R, (*c*) case VM11 and (*d*) case VM21, and (*b*) the corresponding local magnification for case R. The black dashed lines mark the position of the reference point. The blue dash-dot-dotted lines mark the inclination angle of the correlation.

does not alter the primary downstream propagation structure, it selectively modulates the 'long-extent' coherence of the pressure field, with mode (1, 1) panel vibration uniquely enabling traceable spatiotemporal connectivity between the separation region and the far downstream turbulence.

3.4. *Modal analysis: wall pressures and their association with coherent structures*

In this subsection, we further utilise the dynamic mode decomposition (DMD) proposed by Schmid (2010) to explore the spatial organisation of the wall pressure fluctuations at dominant frequencies. The basic principles and procedures are briefly given as follows.

The basic presumption of DMD is that the temporal evolution of the flow field can be approximated by the linear system. Specifically, for a snapshot sequence with N samples from experiments or numerical simulations, described as $\{f_1, f_2, \ldots, f_N\}$, suppose that there exists a linear dynamic system that can map the ith snapshot to the $(i+1)$th snapshot:

$$f_{i+1} = A_D f_i, \tag{3.4}$$

https://doi.org/10.1017/jfm.2026.12068 Published online by Cambridge University Press

where A_D is the evolving matrix of the dynamic system. This mapping relationship can be formulated in matrix form as

$$F_2 = A_D F_1, \tag{3.5}$$

where $F_1 = [f_1, f_2, \ldots, f_{N-1}]$ and $F_2 = [f_2, f_3, \ldots, f_N]$. Matrix A_D is unknown and is difficult to be directly calculated by employing the pseudo-inverse of F_1 in (3.5), for such an operation would render the solution severely ill-conditioned. Therefore, a reduced-order decomposition of matrix F_1 is usually adopted to correctly solve the eigenvalue problem. Performing singular value decomposition on F_1, (3.5) can be expressed as

$$F_2 = A_D U_D \Sigma V_D^H, \tag{3.6}$$

where Σ is a diagonal matrix of rank r (usually $r = N$, for the data points in the column vector are usually much larger than the number of time instants), with non-zero singular values along its main diagonal. Here, U_D and V_D are unitary matrices that are composed of orthogonal modes, satisfying $U_D^H U_D = I$ and $V_D^H V_D = I$. The superscript H indicates the conjugate transpose of a matrix. Also, I is the identity matrix. Projecting A_D onto the basis U_D, (3.6) can be further cast as

$$F_2 = U_D \tilde{A}_D U_D^H U_D \Sigma V_D^H = U_D \tilde{A}_D \Sigma V_D^H, \tag{3.7}$$

where $\tilde{A}_D$ has the same eigenvalues as A_D, with $\tilde{A}_D$ calculated using the formula

$$\tilde{A}_D = U_D^H F_2 V_D \Sigma^{-1}. \tag{3.8}$$

The eigenvalues μ_j ($j = 1, 2, \ldots, r$) and eigenvectors w_j of the matrix $\tilde{A}_D$ are obtained by solving the eigenvalue problem

$$\begin{aligned} &\tilde{A}_D W_D = W_D N, \\ &N = \text{diag}\,(\mu_1, \mu_2, \ldots, \mu_r), \\ &W_D = [w_1, w_2, \ldots, w_r]. \end{aligned} \tag{3.9}$$

The eigenmodes are then obtained as

$$\Phi_D = U_D W_D. \tag{3.10}$$

Therefore, the snapshot at any time i can be approximated as

$$f_i = A_D f_{i-1} = U_D \tilde{A}_D U_D^H f_{i-1} = \Phi_D N^{i-1} \alpha_D, \tag{3.11}$$

where the DMD mode amplitude vector is $\alpha_D = W_D^{-1} U_D^H f_1$. This formula can be simplified to

$$f_i = \sum_{j=1}^{r} \phi_j (\mu_j)^{i-1} \alpha_j, \tag{3.12}$$

where α_j is the jth element of the vector α_D, and ϕ_j is the jth column vector of matrix Φ_D.

Due to the non-orthogonal feature of the eigenvectors in this method, prior knowledge of the fluid physical properties is still required to extract the dominant DMD modes, especially for the flows with strong unsteadiness. To address this issue, Kou & Zhang (2017) proposed a selection criterion for the dominant DMD modes. The unsteady flow field can be described as a summation of the normalised DMD modes multiplied by the corresponding time coefficients. Equation (3.12) can be rewritten as

$$f_i = \sum_{j=1}^{r} b_{ij}(t) \phi_j, \tag{3.13}$$

https://doi.org/10.1017/jfm.2026.12068 Published online by Cambridge University Press

where b_{ij} is the time coefficient of the jth normalised DMD mode of the ith snapshot. Therefore, the influence of the jth DMD mode on the entire sample space, marked by the symbol I_j, can be evaluated by integrating $|b_{ij}|$ over time:

$$I_j = \int_{i=1}^{N} |b_{ij}| \Delta t = \sum_{i=1}^{N} \left| \alpha_j (\mu_j)^{i-1} \right| \left\| \phi_j \right\|_F^2 \Delta t. \tag{3.14}$$

According to this, the dominant DMD modes can be identified.

As established by Adler & Gaitonde (2020), wall pressure fluctuations in STBLI flows display three dynamic characteristics, dictated by their dominant frequencies: (i) low-frequency ($f\delta/U_\infty \sim O(0.0033)$) fluctuations associated with bubble breathing, (ii) mid-frequency ($f\delta/U_\infty \sim O(0.1)$) fluctuations associated with the shedding vortices, reminiscent of Kelvin–Helmholtz instability due to the separated shear layer, and (iii) high-frequency ($f\delta/U_\infty \gtrsim O(1)$) fluctuations pertaining to turbulent motions within the boundary layer. In light of this, the current work defines analogous frequency ranges: low frequency ($f\delta/U_\infty \leq 0.022$), medium frequency ($0.022 < f\delta/U_\infty \leq 0.22$) and high frequency ($f\delta/U_\infty > 0.22$).

The wall pressure fluctuations can be associated with the coherent structures in the flow field, by analysing the correlation between velocity fluctuations u' and pressure fluctuations p'. To extract the DMD modes of u' and p' at the exact same frequency, we perform DMD on the data matrix that is composed of u' and p' in the range $x/\delta \geq -5$ (Shinde *et al.* 2022). The 1075 data samples are collected with time interval $0.0058 L_{ref}/u_\infty$, covering the time period $6.235 L_{ref}/u_\infty$. The u' and p' values are non-dimensionalised by the corresponding free-stream values. Prior to DMD computation, the data were pre-multiplied by the mesh volume to eliminate the influence of grid inhomogeneity.

Figure 17 shows the distribution of I_j across all positive-frequency DMD modes, with dominant modes in each frequency range highlighted by red dots. In the rigid wall case, the I_j peak occurs in the low-frequency range and is considerably higher than those in the mid- and high-frequency ranges, indicating that low-frequency oscillations dominate u' and p' in the flow field. This finding aligns with previous studies of Priebe & Martín (2012). When panel vibration is introduced, the DMD mode ϕ_1 with a frequency close to the panel vibration frequency exhibits a significantly stronger influence over the entire sample space, surpassing the contributions of other DMD modes. In the high-frequency range, the I_j values of DMD modes decrease with the frequency increases, suggesting that the high-frequency components associated with the turbulent boundary layer gradually lose their influence on the evolution of u' and p'. In vibration cases, the vibration slightly concentrates the I_j distribution around a specific DMD mode ϕ_2 in the mid-frequency range, while its effect remains negligible in the high-frequency range, similar to observation in the rigid wall case. Therefore, the low-frequency DMD mode ϕ_1 represents the mode associated with the panel vibration frequency, whereas the mid-frequency DMD mode ϕ_2 and the high-frequency DMD mode ϕ_3, the most-energetic modes within their respective frequency bands, are provided as illustrative examples for the mid- and high-frequency ranges, respectively.

We first consider the wall pressure fluctuations separately. To examine the influence of wall panel vibration on the structural features of low-frequency pressure fluctuations, figure 18 presents the real and negative imaginary parts of the low-frequency DMD mode ϕ_1 for the wall pressure fluctuations under different vibrating panel conditions. When the growth rates of DMD modes are neglected, the real and negative imaginary parts correspond to the two discrete phase angles 0 and $\pi/2$ in the temporal evolution

https://doi.org/10.1017/jfm.2026.12068 Published online by Cambridge University Press

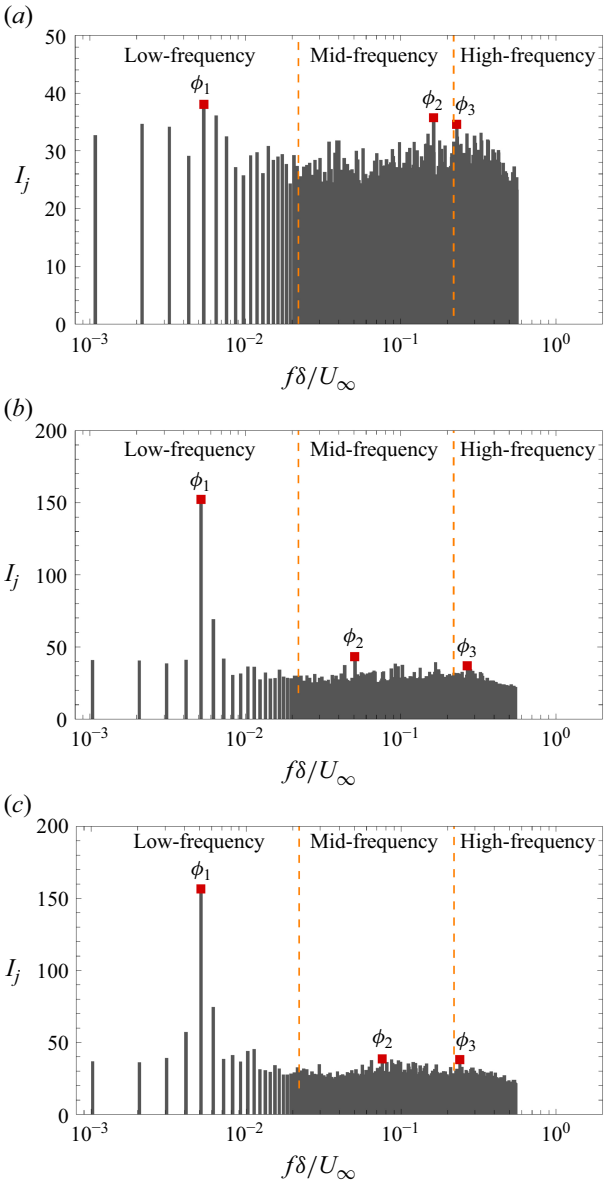


Figure 17. Integration of the time coefficients of the positive-frequency DMD modes of u' and p' for (*a*) case R, (*b*) case VM11 and (*c*) case VM21.

of the DMD mode (Pasquariello *et al.* 2017). In the rigid wall case, regions of high-level wall pressure fluctuations are mainly concentrated within the interaction zone, as low-frequency fluctuations are associated with the unsteady motions of shock wave and separation bubble. Near the separation point, the fluctuations exhibit opposite signs to those inside the separation bubble, and they reach their maximum values almost simultaneously. It can be inferred that the pressure fluctuations propagate downstream and begin to break down into smaller structures in the vicinity of the trailing edge of the separated bubble.

https://doi.org/10.1017/jfm.2026.12068 Published online by Cambridge University Press

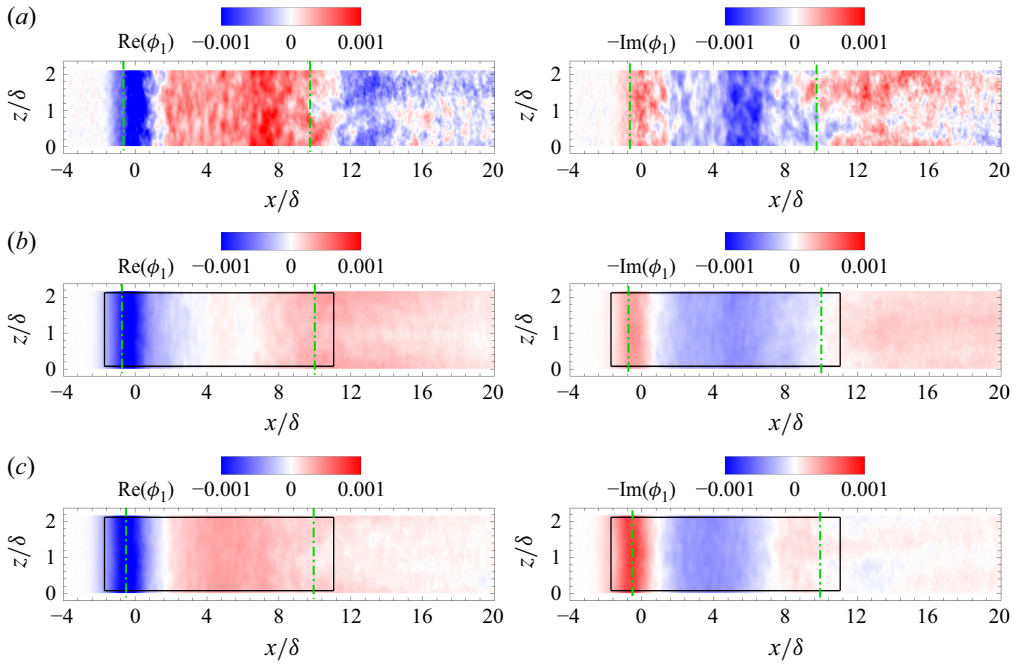


Figure 18. Real and negative imaginary parts of low-frequency DMD mode ϕ_1 for the wall pressure fluctuations in (*a*) case R, (*b*) case VM11 and (*c*) case VM21. The black solid lines mark the vibration range of the panel. The green dash-dotted lines denote the streamwise range of the mean flow separation.

When the wall panel vibrates, the streamwise extent of high-level region near the mean separation point increases due to the expanded motion range of the separation shock wave (recall figure 9). However, the downstream evolution of the pressure fluctuations differs among vibrating panel cases. In case VM11 with the vibrating mode (1, 1), wall pressure fluctuations are generated near the separation point, propagate downstream, gradually covering the entire panel, and then continue to propagate beyond the interaction zone while gradually decaying. Given that the frequency of the DMD mode ϕ_1 essentially coincides with weak low-frequency signals in the frequency spectra (figure 6), it can be inferred that these weak low-frequency signals downstream of the panel in case VM11 result from the movement of the separation shock wave. This finding further supports the conclusion drawn from the two-point correlation analysis (figure 16).

In contrast to case VM11, downstream of the interaction zone, the pressure fluctuations amplitude in case VM21 with the vibration mode (2, 1) remains relatively low and gradually decays, consistent with the discussion regarding figure 10. Considering that vibrating mode (2, 1) induces asymmetric deformation between its front and rear sections, where the wall pressure evolves in opposite manners on the concave and convex surfaces, the resulting destructive interference arises from the opposing deformations of the rear and front halves of the panel. This mechanism also weakens low-frequency pressure fluctuations in the downstream region, making them insufficiently high in the PSD results, as noted in the discussion of figure 6.

Figure 19 displays the real and negative imaginary parts of the DMD mode ϕ_2 for the wall pressure fluctuations in the mid-frequency range. In the rigid wall case, pressure fluctuations originating from the separation point gradually form coherent spanwise-extended structures. These structures subsequently elongate in the streamwise direction, but begin to break down in the rear portion of the interaction zone. Finally, downstream of

https://doi.org/10.1017/jfm.2026.12068 Published online by Cambridge University Press

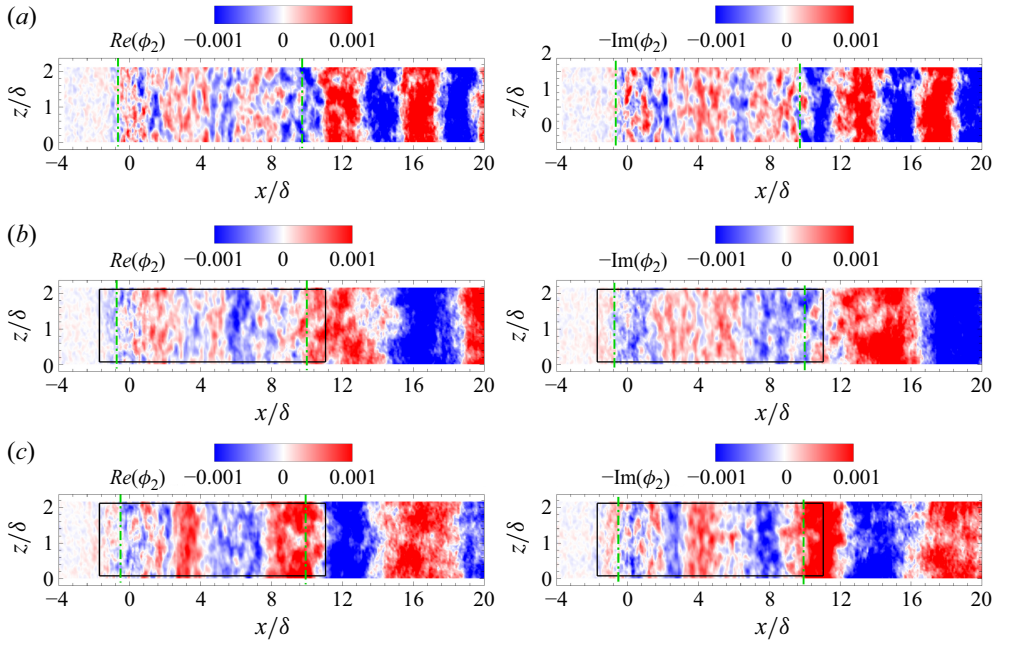


Figure 19. Real and negative imaginary parts of mid-frequency DMD mode ϕ_2 for the wall pressure fluctuations in (*a*) case R, (*b*) case VM11 and (*c*) case VM21. The black solid lines mark the vibration range of the panel. The green dash-dotted lines denote the streamwise range of the mean flow separation.

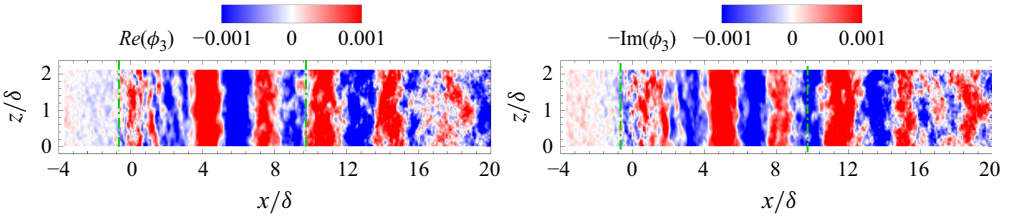


Figure 20. Real and negative imaginary parts of high-frequency DMD mode ϕ_3 for the wall pressure fluctuations in case R. The black solid lines mark the vibration range of the panel. The green dash-dotted lines denote the streamwise range of the mean flow separation.

reattachment point, the structures reassemble and enlarge. When the panel is subjected to mode (1, 1) panel vibration, the pressure structural evolution process in the DMD mode shows no significant differences from the rigid wall case. In contrast, for case VM21 with mode (2, 1) panel vibration, structural fragmentation is not observed in the rear portion of the interaction zone. As indicated by the phase-averaged results in § 3.2, the separation bubble in case VM21 primarily moves in the upstream–downstream direction, while in case VM11, it exhibits expansion–contraction behaviour similar to that in the rigid wall case, though with increased amplitude. Therefore, it can be concluded that the overall upstream–downstream motion of the separation bubble suppresses the breakdown of the mid-frequency structures in the rear part of the interaction zone. Since the high-frequency DMD mode ϕ_3 for the wall pressure fluctuations shows nearly identical characteristics with all cases, only the results from case R are plotted in figure 20 for conciseness. Meanwhile, this indicates that the influence of low-frequency vibration applied to the wall panel on the high-frequency structures organisation of the pressure fluctuations is negligible.

https://doi.org/10.1017/jfm.2026.12068 Published online by Cambridge University Press

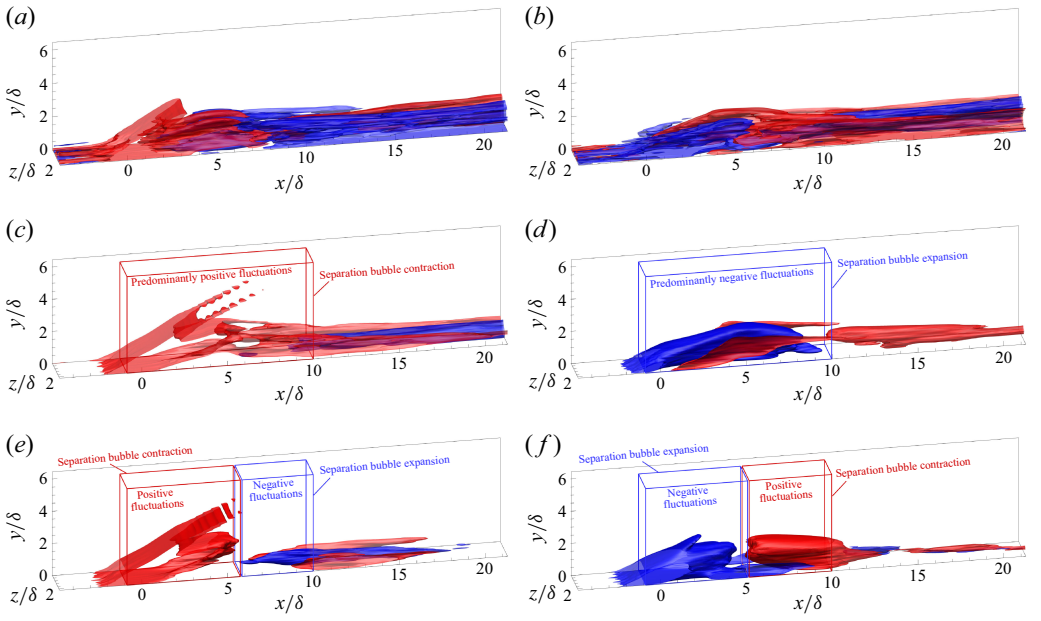


Figure 21. Iso-surfaces of low-frequency DMD mode ϕ_1 for velocity fluctuations in (*a*,*b*) case R, (*c*,*d*) case VM11 and (*e*,*f*) case VM21, for (*a*,*c*,*e*) real part, (*b*,*d*,*f*) negative imaginary part. The values of the red and blue iso-surfaces are 0.0001, −0.0001, respectively.

To further elucidate the origin of wall pressure fluctuations, we analyse the coherent flow structures at low, mid and high frequencies. Figure 21 presents the three-dimensional iso-surfaces of both the real and negative imaginary parts for the DMD mode ϕ_1 for u' under different vibrating panel conditions. A key finding from the baseline rigid wall case R is the distinct spatial organisation revealed by this DMD mode. The generation of a region with positive streamwise velocity fluctuation immediately upstream of the separation shock provides direct visual evidence that the DMD mode corresponds to a downstream displacement of the shock front. This kinematic motion is the physical mechanism responsible for the concurrent negative pressure fluctuation near the shock foot, a relationship previously inferred from the pressure field in figure 18(*a*). More significantly, downstream of the interaction zone, the DMD mode exhibits a pair of counter-rotating, streamwise-elongated structures in the velocity fluctuation field. This specific pattern is a clear signature of large-scale, coherent streamwise vortices, structurally analogous to Görtler-like vortices, which are identified here as a dominant carrier of low-frequency energy in the separated flow region (Pasquariello *et al.* 2017; Shinde 2025).

The introduction of wall panel vibration induces a marked spatial reorganisation of the coherent structures within the interaction zone, with the specific mode dictating the primary response. For case VM11 (mode (1, 1) vibration), the low-frequency DMD mode ϕ_1 reveals a single, dominant structure of either positive or negative streamwise velocity fluctuation spanning the interaction region. This spatial pattern directly corresponds to a global contraction or expansion of the separation bubble, confirming its volumetric 'breathing' mode identified in prior analyses. In stark contrast, for case VM21 (mode (2, 1) vibration), the DMD mode consistently exhibits a counter-rotating pair of streamwise-aligned fluctuation structures. This signature is the definitive modal footprint of the bubble undergoing a coherent streamwise oscillatory motion, i.e. a fore-and-aft sloshing. Critically, the frequency of this dominant DMD mode is identical to the imposed panel

https://doi.org/10.1017/jfm.2026.12068 Published online by Cambridge University Press

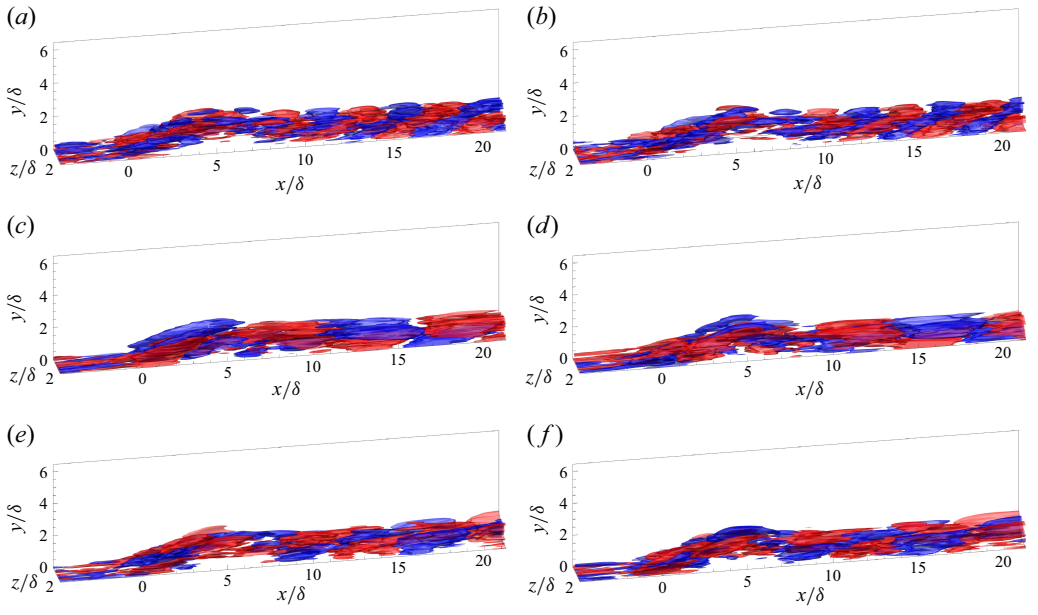


Figure 22. Iso-surfaces of mid-frequency DMD mode ϕ_2 for velocity fluctuations in (*a*,*b*) case R, (*c*,*d*) case VM11 and (*e*,*f*) case VM21, for (*a*,*c*,*e*) real part, (*b*,*d*,*f*) negative imaginary part. The values of the red and blue iso-surfaces are 0.0001, -0.0001, respectively.

vibration frequency. This direct spectral correspondence provides powerful, independent modal evidence that firmly corroborates the phase-averaged dynamics shown in figures 11 and 12, confirming the vibration as the direct driver of these distinct low-frequency motions. A further significant finding concerns the flow downstream. Under both vibrating conditions, the pair of coherent streamwise structures (akin to the Görtler-like vortices), prominent in the rigid wall baseline, is substantially attenuated or absent. This indicates that the panel's low-frequency vibration suppresses the inherent spanwise instability responsible for generating these vortices downstream of the interaction zone. The modified bubble dynamics, either volumetric change or streamwise oscillation, tends to stabilise the shear layer, thereby mitigating this secondary instability mechanism.

Figure 22 presents the iso-surfaces of real and negative imaginary parts for a representative mid-frequency DMD mode ϕ_2 for u' under different vibrating panel conditions. Similar to high-frequency DMD mode ϕ_3 for wall pressure fluctuations, the DMD mode ϕ_3 for u' is largely consistent across all cases. Accordingly, only the results for case R are presented in figure 23. In the rigid wall baseline, both mid- and high-frequency coherent structures originate from the incoming turbulent boundary layer. They are subsequently lifted and amplified within the separation shear layer before propagating downstream along the recirculation boundary layer, characterising the natural turbulence modulation through the interaction zone. A key finding is the differential impact of panel vibration on these frequency regimes. While the overall spatial organisations of these turbulent structures remain largely unaltered, a significant scale modification is observed specifically for the mid-frequency structures. Their characteristic spatial scale increases discernibly due to the downward shift in the dominant DMD mode frequency under vibration. This observation is consistent with the energy distribution shown in figure 17, where the spectrum in the mid-frequency range becomes slightly concentrated around specific low- to mid-frequency DMD modes. This indicates that

https://doi.org/10.1017/jfm.2026.12068 Published online by Cambridge University Press

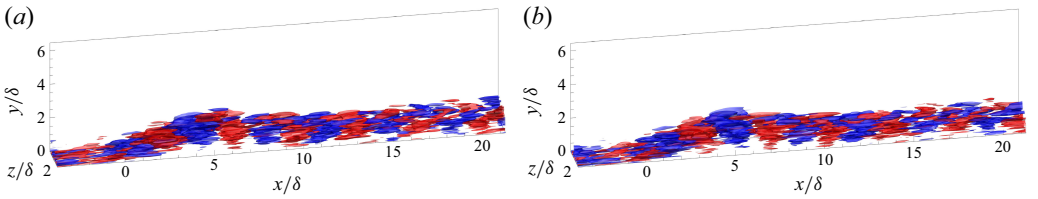


Figure 23. Iso-surfaces of high-frequency DMD mode ϕ_3 for velocity fluctuations in case R, for (a,c,e) real part, (b,d,f) negative imaginary part. The values of the red and blue iso-surfaces are 0.0001, −0.0001, respectively.

the applied low-frequency panel vibration can slightly excite or reinforce low- to mid-frequency coherent motions within the turbulence. In contrast, the topology and energy content of the high-frequency structures show negligible sensitivity to the low-frequency forcing, suggesting a decoupling between the imposed large-scale motion and the fine-scale turbulent dynamics. Henceforth, the primary influence of the low-frequency panel vibration on the turbulent field is not a restructuring of small-scale eddies, but a selective, frequency-dependent modulation that preferentially affects the energy-containing scales in the low- and mid-frequency ranges, thereby altering the spectral distribution of turbulent kinetic energy.

4. Conclusion

In this paper, by conducting direct numerical simulations of an oblique shock wave/turbulent boundary layer interaction (STBLI) at free-stream Mach number 2.9, we systematically investigate the influence mechanisms of wall-pressure fluctuations by two low-frequency vibration modes of a flexible panel: mode (2, 1) and mode (1, 1). The vibration frequency is set to the dominant frequency of the low-frequency pressure fluctuations observed in the rigid wall case to examine potential resonance effects.

The results indicate that while the panel vibration has a limited effect on the mean flow field, it significantly modulates the characteristics of unsteady pressure fluctuations. Pre-multiplied spectral analysis reveals that the vibration not only greatly enhances the intensity and spatial extent of the original low-frequency signal near the mean separation point, but also excites a distinct new low-frequency signal synchronised with the vibration frequency within the interaction zone. This new signal decays gradually in the streamwise direction, with a faster decay rate observed for vibration mode (2, 1) compared to vibration mode (1, 1).

The primary innovation of this work lies in elucidating the differences in separation bubble dynamics driven by different vibration modes. Phase averaging and dynamic mode decomposition (DMD) of velocity fluctuations jointly confirm that mode (2, 1) vibration primarily induces a streamwise oscillation of the separation bubble, whereas mode (1, 1) amplifies its inherent expansion/contraction (‘breathing’) motion. The bubble motion is synchronised with the panel vibration for mode (2, 1), but exhibits a phase lag of one-eighth of a vibration period for mode (1, 1). These two distinct motion patterns force quasi-periodic oscillations of the separation shock wave, modulate the pressure plateau, and cause enhanced low-frequency pressure signals to manifest not only at the conventional separation point but also at various mid-panel locations.

Correlation analysis and DMD further indicate that the weak low-frequency pressure fluctuations downstream of the panel originate from the enhanced fluctuations near the separation point. However, for mode (2, 1), the cancelling effect caused by the opposite

https://doi.org/10.1017/jfm.2026.12068 Published online by Cambridge University Press

deformations of the front and rear panel halves weakens these downstream fluctuations, making them difficult to detect. Furthermore, because mode (2, 1) transitions the primary bubble motion to streamwise oscillation, the coherent structures of mid-frequency pressure fluctuations remain intact in the posterior part of the interaction region, without observable fragmentation. The applied low-frequency vibration has a negligible influence on high-frequency pressure fluctuations for both modes.

Variations of the panel vibration amplitude within a reasonable range (excluding extremely large amplitudes that induce additional flow separation) exert no qualitative influence on the present results. In addition, the friction Reynolds number barely affects the low-frequency dynamics of STBLI (Laguarda *et al.* 2024*b*). Consequently, although only one vibration amplitude and one friction Reynolds number are considered in the current work, the derived conclusions retain a certain degree of generality.

In summary, by imposing panel vibration within the interaction region, this study reveals the modulation mechanism of wall panel vibration on low-frequency oscillation characteristics. These modifications establish that the spatial pattern of the vibration mode is the primary factor dictating the flow response mechanism, whether streamwise translation or volumetric breathing. Future work will be dedicated to the two-way coupled simulations of turbulent boundary layer over a flexible panel.

Funding. This work was supported by the National Natural Science Foundation of China (grant nos 92371115, 11902345, 12102447, U2341241, 12422211) and the National Numerical Wind Tunnel Project.

Declaration of interests. The authors report no conflict of interest.

References

Acosta, A.R. & Austin, J.M. 2024 Experimental investigation of an impinging shock–boundary layer interaction on a compliant panel in Mach 4 flow. *AIAA Paper* 2024-1153. AIAA.

Adler, M.C. & Gaitonde, D.V. 2020 Dynamics of strong swept-shock/turbulent-boundary-layer interactions. *J. Fluid Mech.* **896**, A29.

Babinsky, H. & Harvey, J.K. 2011 *Shock Wave–Boundary-Layer Interactions*. Cambridge University Press.

Beresh, S.J., Clemens, N.T. & Dolling, D.S. 2002 Relationship between upstream turbulent boundary-layer velocity fluctuations and separation shock unsteadiness. AIAA J. **40** (12), 2412–2422.

Bernardini, M. & Pirozzoli, S. 2011 Wall pressure fluctuations beneath supersonic turbulent boundary layers. *Phys. Fluids* **23** (8), 085102.

Bernardini, M., Pirozzoli, S. & Grasso, F. 2011 The wall pressure signature of transonic shock/boundary layer interaction. *J. Fluid Mech.* **671**, 288–312.

Bernardini, M., Posta, D.G., Salvadore, F. & Martelli, E. 2023 Unsteadiness characterisation of shock wave/turbulent boundary-layer interaction at moderate Reynolds number. *J. Fluid Mech.* **954**, A43.

Bookey, P., Wyckham, C. & Smits, A. 2005 Experimental investigations of Mach 3 shock-wave turbulent boundary layer interactions. *AIAA Paper* 2005-4899. AIAA.

Boyer, N.R., McNamara, J.J., Gaitonde, D.V., Barnes, C.J. & Visbal, M.R. 2018 Features of shock-induced panel flutter in three-dimensional inviscid flow. *J. Fluids Struct.* **83**, 490–506.

Boyer, N.R., McNamara, J.J., Gaitonde, D.V., Barnes, C.J. & Visbal, M.R. 2021 Features of panel flutter response to shock boundary layer interactions. *J. Fluids Struct.* **101**, 103207.

Cai, H., Yu, M., Sun, D., Ye, Z., Liu, P. & Yuan, X. 2022 Wall pressure fluctuations in supersonic boundary layers over compression ramps with different turning angles. *Phys. Fluids* **34** (12), 126105.

Ceci, A., Palumbo, A., Larsson, J. & Pirozzoli, S. 2024 Low-frequency unsteadiness in hypersonic swept shock wave–boundary layer interactions. *Phys. Rev. Fluids* **9** (5), 054603.

Clemens, N.T. & Narayanaswamy, V. 2014 Low-frequency unsteadiness of shock wave/turbulent boundary layer interactions. *Annu. Rev. Fluid Mech.* **46** (1), 469–492.

Delery, J.M. 1985 Shock wave/turbulent boundary layer interaction and its control. *Prog. Aerosp. Sci.* **22** (4), 209–280.

Deng, X. & Zhang, H. 2000 Developing high-order weighted compact nonlinear schemes. *J. Comput. Phys.* **165** (1), 22–44.

https://doi.org/10.1017/jfm.2026.12068 Published online by Cambridge University Press

DOLLING, D.S. 2001 Fifty years of shock-wave/boundary-layer interaction research: what next? *AIAA J.* **39** (8), 1517–1531.

DUAN, L., CHOUDHARI, M.M. & WU, M. 2014 Numerical study of acoustic radiation due to a supersonic turbulent boundary layer. *J. Fluid Mech.* **746**, 165–192.

DUPONT, P., HADDAD, C. & DEBIEVE, J. 2006 Space and time organization in a shock-induced separated boundary layer. *J. Fluid Mech.* **559**, 255–277.

DUSSAUGE, J.-P., DUPONT, P. & DEBIÈVE, J.-F. 2006 Unsteadiness in shock wave boundary layer interactions with separation. *Aerosp. Sci. Technol.* **10** (2), 85–91.

FANG, J., ZHELTOVODOV, A.A., YAO, Y., MOULINEC, C. & EMERSON, D.R. 2020 On the turbulence amplification in shock-wave/turbulent boundary layer interaction. *J. Fluid Mech.* **897**, A32.

GAITONDE, D.V. 2015 Progress in shock wave/boundary layer interactions. *Prog. Aerosp. Sci.* **72**, 80–99.

GANAPATHISUBRAMANI, B., CLEMENS, N.T. & DOLLING, D.S. 2007 Effects of upstream boundary layer on the unsteadiness of shock-induced separation. *J. Fluid Mech.* **585**, 369–394.

GANAPATHISUBRAMANI, B., CLEMENS, N.T. & DOLLING, D.S. 2009 Low-frequency dynamics of shock-induced separation in a compression ramp interaction. *J. Fluid Mech.* **636**, 397–425.

GOTTLIEB, S. & SHU, C. 1998 Total variation diminishing Runge–Kutta schemes. *Maths Comput.* **67** (221), 73–85.

HIRAI, R. & KAWAI, S. 2023 Wall pressure fluctuations in wall heated and cooled shock wave and turbulent boundary layer interactions. *Intl J. Heat Fluid Flow* **103**, 109205.

JI, Y., JIANG, Z., ZHU, X., YANG, X. & XIA, Z. 2025 Analysis of low-frequency characteristics in shock wave–turbulent boundary layer interaction through pressure fluctuation decomposition. *Phys. Fluids* **37** (8), 086121.

KIMMEL, E.S., HUANG, D., SHARMA, V., SINGH, J., RAMAN, V. & FRIEDMANN, P.P. 2025 Turbulence and upstream shock wave–boundary layer interaction effects on compliant structures. *AIAA J.* **63** (9), 3641–3653.

KOU, J. & ZHANG, W. 2017 An improved criterion to select dominant modes from dynamic mode decomposition. *Eur. J. Mech. B/Fluids* **62**, 109–129.

LAGUARDA, L., HICKEL, S., SCHRIJER, F.F.J. & VAN OUDHEUSDEN, B.W. 2024*a* Shock-wave/turbulent boundary-layer interaction with a flexible panel. *Phys. Fluids* **36** (1), 016120.

LAGUARDA, L., HICKEL, S., SCHRIJER, F.F.J. & VAN OUDHEUSDEN, B.W. 2024*b* Reynolds number effects in shock-wave/turbulent boundary-layer interactions. *J. Fluid Mech.* **989**, A20.

LIAO, F. & YE, Z. 2015 Extending geometric conservation law to cell-centered finite difference methods on moving and deforming grids. *J. Comput. Phys.* **303**, 212–221.

MARTIN, M.P., PRIEBE, S. & HELM, C.M. 2016 Upstream and downstream influence on STBLI instability. *AIAA Paper* 2016-3341. AIAA.

PASQUARIELLO, V., HICKEL, S. & ADAMS, N.A. 2017 Unsteady effects of strong shock-wave/boundary-layer interaction at high Reynolds number. *J. Fluid Mech.* **823**, 617–657.

PIPONNIAU, S., DUSSAUGE, J., DEBIEVE, J. & DUPONT, P. 2009 A simple model for low-frequency unsteadiness in shock-induced separation. *J. Fluid Mech.* **629**, 87–108.

PIROZZOLI, S., BERNARDINI, M. & GRASSO, F. 2010 Direct numerical simulation of transonic shock/boundary layer interaction under conditions of incipient separation. *J. Fluid Mech.* **657**, 361–393.

PIROZZOLI, S., GRASSO, F. & GATSKI, T.B. 2004 Direct numerical simulation and analysis of a spatially evolving supersonic turbulent boundary layer at $M = 2.25$. *Phys. Fluids* **16** (3), 530–545.

PRIEBE, S. & MARTÍN, M.P. 2012 Low-frequency unsteadiness in shock wave–turbulent boundary layer interaction. *J. Fluid Mech.* **699**, 1–49.

PRIEBE, S., WU, M. & MARTÍN, M.P. 2009 Direct numerical simulation of a reflected-shock-wave/turbulent-boundary-layer interaction. *AIAA J.* **47** (5), 1173–1185.

RINGUETTE, M.J., BOOKEY, P., WYCKHAM, C. & SMITS, A.J. 2009 Experimental study of a Mach 3 compression ramp interaction at $Re_{h}eta = 2400$. *AIAA J.* **47** (2), 373–385.

SCHMID, P.J. 2010 Dynamic mode decomposition of numerical and experimental data. *J. Fluid Mech.* **656**, 5–28.

SCIACOVELLI, L., PASSIATORE, D., CINNELLA, P. & PASCAZIO, G. 2021 Assessment of a high-order shock-capturing central-difference scheme for hypersonic turbulent flow simulations. *Comput. Fluids* **230**, 105134.

SHINDE, V. 2025 Distributed-parallel proper orthogonal/dynamic mode decompositions of large flow data. *Comput. Phys. Commun.* **313**, 109644.

SHINDE, V., MCNAMARA, J. & GAITONDE, D. 2022 Dynamic interaction between shock wave turbulent boundary layer and flexible panel. *J. Fluids Struct.* **113**, 103660.

SHINDE, V., MCNAMARA, J., GAITONDE, D., BARNES, C. & VISBAL, M. 2019 Transitional shock wave boundary layer interaction over a flexible panel. *J. Fluids Struct.* **90**, 263–285.

https://doi.org/10.1017/jfm.2026.12068 Published online by Cambridge University Press

SOUVEREIN, L.J., DUPONT, P., DEBIEVE, J., DUSSAUGE, J., VAN OUDHEUSDEN, B.W. & SCARANO, F. 2010 Effect of interaction strength on unsteadiness in shock-wave-induced separations. *AIAA J.* **48** (7), 1480–1493.

SPOTTSWOOD, S.M., EASON, T. & BEBERNISS, T. 2012 Influence of shock-boundary layer interactions on the dynamic response of a flexible panel. In *International Conference on Noise and Vibration Engineering (ISMA) / International Conference on Uncertainty in Structural Dynamics (USD), Leuven, Belgium*, pp. 603–616. ISMA/USD.

TONG, F., DUAN, J., ZHOU, G. & LI, X. 2021 Statistical characteristics of pressure fluctuation in shock wave and turbulent boundary layer interaction. *Chin. J. Theor. Appl. Mech.* **53** (7), 1829–1841.

TRIPATHI, A., GUSTAVSSON, J., SHOELE, K. & KUMAR, R. 2024 Effect of shock impingement location on the fluid–structure interactions over a compliant panel. *Shock Waves* **34** (1), 1–19.

TRIPATHI, A., SHEEHAN, M., GUSTAVSSON, J., SHOELE, K. & KUMAR, R. 2023 Effect of panel compliance on shockwave boundary layer interaction at Mach 2. *AIAA Paper* 2023-3852. AIAA.

VANSTONE, L. & CLEMENS, N.T. 2019 Proper orthogonal decomposition analysis of swept-ramp shock-wave/boundary-layer unsteadiness at Mach 2. *AIAA J.* **57** (8), 3395–3409.

VARIGONDA, S.V. & NARAYANASWAMY, V. 2023 Fluid structure interactions generated by an oblique shock impinging on a thin elastic panel. *J. Fluids Struct.* **119**, 103890.

VISBAL, M. 2014 Viscous and inviscid interactions of an oblique shock with a flexible panel. *J. Fluids Struct.* **48**, 27–45.

WANG, Q., WANG, Z., SUN, M., YANG, R., ZHAO, Y. & HU, Z. 2019 The amplification of large-scale motion in a supersonic concave turbulent boundary layer and its impact on the mean and statistical properties. *J. Fluid Mech.* **863**, 454–493.

WANG, Q., WANG, Z. & ZHAO, Y. 2016 On the impact of adverse pressure gradient on the supersonic turbulent boundary layer. *Phys. Fluids* **28** (11), 116101.

WU, M. & MARTIN, M.P. 2007 Direct numerical simulation of supersonic turbulent boundary layer over a compression ramp. *AIAA J.* **45** (4), 879–889.

WU, M. & MARTIN, M.P. 2008 Analysis of shock motion in shockwave and turbulent boundary layer interaction using direct numerical simulation data. *J. Fluid Mech.* **594**, 71–83.

WU, X. & MOIN, P. 2009 Direct numerical simulation of turbulence in a nominally zero-pressure-gradient flat-plate boundary layer. *J. Fluid Mech.* **630**, 5–41.

ZHANG, Y., TAN, H., TIAN, F. & ZHUANG, Y. 2014 Control of incident shock/boundary-layer interaction by a two-dimensional bump. *AIAA J.* **52** (4), 767–776.

ZHONG, D., LIXU, W. & NING, G.E. 2021 Reflected shock/turbulent boundary layer interaction structure analysis based on large eddy simulation. *Chin. J. Aeronaut.* **34** (5), 364–372.

https://doi.org/10.1017/jfm.2026.12068 Published online by Cambridge University Press